

# Natural Convection Flow of a Hybrid Nanofluid in a Square Enclosure Partially Filled with a Porous Medium Using a Thermal Non-Equilibrium Model

**Basil Mahdi Al-Srayyih<sup>1,2,a</sup>, Shian Gao<sup>1</sup>, Salam Hadi Hussain<sup>3</sup>**

<sup>1</sup> Department of Engineering, University of Leicester, Leicester LE1 7RH, United Kingdom.

<sup>2</sup> Department of Mechanical Engineering, College of Engineering, University of Babylon, Babylon Province, Iraq.

<sup>3</sup> Department of Automobile Engineering, College of Engineering Al-Musayab, University of Babylon, Babylon Province, Iraq.

Buoyancy-driven flow inside a superposed enclosure filled with composite porous-hybrid nanofluid layers was investigated numerically using a local thermal non-equilibrium (LTNE) model for the heat transfer between the fluid and the solid phases. The bottom wall of the enclosure was partly heated to provide a heat flux, while the other parts of the wall were thermally insulated. The top and vertical walls of the enclosure were maintained at constant cold temperatures. The Darcy-Brinkmann model was adopted to model the flow inside the porous layer. The Galerkin finite element method was used to solve the governing equations using the SIMPLE (Semi-Implicit Method for Pressure Linked Equations) algorithm. The selected parameters are presented for the Rayleigh number ( $Ra$ ),  $10^3 \leq Ra \leq 10^7$ , the Darcy number ( $Da$ ),  $10^{-7} \leq Da \leq 1$ , the porous layer thickness ( $S$ ),  $0 \leq S \leq 1$ , the modified conductivity ratio ( $\gamma$ ),  $10^{-1} \leq \gamma \leq 10^4$ , the interphase heat transfer coefficient ( $H$ ),  $10^{-1} \leq H \leq 1000$ , the heat source length ( $B$ ), 0.2, 0.4, 0.6, 0.8 and 1, and the nanoparticle volume fraction ( $\phi$ ),  $0 \leq \phi \leq 0.2$ . It has been concluded that the rate of heat transfer of hybrid nanofluid ( $Cu - Al_2O_3$ / water) is higher than with the pure fluid. Further, at  $Ra \leq 10^5$  the heat transfer rate maintains its a maximum value when  $S$  reaches the critical value ( $S = 0.3$ ). The values of  $S$ ,  $Da$ , and  $B$  were found to have a significant effect on the heat removal from the heat source. Increasing the values of  $\gamma$  and  $H$  can strongly enhance the heat transfer rate and satisfy the thermal equilibrium case.

**Keywords:** Natural convection, composite hybrid nanofluid-porous layers, non-equilibrium model, isoflux heating

---

<sup>a)</sup> Author to whom correspondence should be addressed: [bmhs2@le.ac.uk](mailto:bmhs2@le.ac.uk) and [basilmh71@yahoo.com](mailto:basilmh71@yahoo.com). Tel: +44 (0)116 252 2874. Fax: +44 (0)116 2522525.

## I. INTRODUCTION

The study of buoyancy-driven heat transfer within a porous enclosure is an important issue in many industrial engineering applications such as heat exchangers, ground-coupled heat pumps, solar collectors, cooling of computers systems, and other electronic equipment <sup>1</sup>. A porous medium has been used to improve heat transfer rates in recent years <sup>2-4</sup>. In these applications, modelling heat transfer within porous enclosures under different boundary conditions, typically using numerical methods, is also important to obtain efficient thermal exchange systems. These systems allow for extensive simulation and analysis prior to manufacture in order to reduce the costs associated with manufacturing tests. Interesting details in this regard can be found in the reference books <sup>5-8</sup>.

Several important studies <sup>9-15</sup> have investigated natural convection within enclosures filled with porous media saturated with a pure fluid as a medium for the heat transfer under different boundary conditions. Other studies have considered natural convection within the superposed layers in which the porous layer is either in a horizontal orientation, such as in <sup>16-19</sup>, or in a vertical orientation, such as in <sup>20-22</sup>. The results of these studies demonstrated that the convective heat transfer inside the enclosure reduced with increasing porous medium layer thickness due to the resistance offered by the porous medium. This resistance can be reduced by increasing the permeability of the porous medium (Darcy number). In addition, Sathe, *et al.*<sup>22</sup> observed that the rate of heat transfer was reduced when the thermal conductivity ratio (fluid/porous) was less than one.

The modern world has witnessed remarkable development in the technology of components and devices. For example, in some applications, these components or devices may increase their temperature due to their electrical resistance, which can sometimes lead to an increased risk of the device generating a fault. This generates the requirement to dissipate the heat from these components. The purpose of thermal management is to ensure the temperature of the system components remains within the design limits, as well as to ensure the control of convective heat transfer using a pure fluid such as air, water, mineral oils, or ethylene glycol as a working fluid; however, a pure fluid may not satisfy the design limits in terms of component temperature. Researchers have been considering several techniques to control fluid flow and heat transfer inside enclosures. One such is that of adding nanoparticles to the pure fluid, which is referred to as a nanofluid technique. The control that this method offers over heat transfer stems from the fact that nanoparticles have greater thermal conductivity than that of the conventional pure fluids. There is an argument about the effect of using this type of fluid

in some cases. Several literature surveys concerning the use of enclosures entirely filled with nanofluids (i.e., no porous medium) can be found in the literature such as references 23-26. Grobler, *et al.*<sup>27</sup> experimentally studied the natural convection in an enclosure completely filled with a porous medium saturated with a nanofluid. They reported that the rate of heat transfer in the presence of the nanofluid was enhanced compared to the pure fluid. A further extension to the above-mentioned fields is that studies of convective heat transfer in a porous cavity saturated with a nanofluid can also found in references such as 28-34. Chamkha and Ismael<sup>3</sup> studied natural convection in a two-dimensional partly filled composite cavity, where the porous medium was vertically orientated and was saturated with a copper-water nanofluid. In this instance, the presence of the nanofluid was found to improve the rate of heat transfer despite the lower permeability of the porous medium (low Darcy number value). Hussain and Rahomey<sup>35</sup> investigated the natural convection inside a superposed square enclosure filled with nanofluid-porous layers, which also contained hot inner cylinders of various geometries. Recently, researchers developed the idea of improving the thermal conductivity of the working fluid by using a new type of nanofluid, which is referred to as a hybrid nanofluid. This type of nanofluid is prepared by suspending dissimilar nanoparticles either in a mixture or composite form in the pure base fluid<sup>36</sup>. Some metallic nanoparticles, such as copper, aluminium, and zinc, provide high thermal conductivity, but are limited in nanofluid-related applications because of their high reactivity and low stability. In addition, whilst non-metallic nanoparticles such as alumina ( $\text{Al}_2\text{O}_3$ ) have lower thermal conductivities than metallic nanoparticles, these types of nanoparticle have other, more preferable physical properties such as high stability and chemical inertness.<sup>36</sup> Interesting reviews of hybrid nanofluids can found in the literature 37-41. Several experimental studies 42-45 have been carried out into the new technology of hybrid nanofluids. Suresh, *et al.*<sup>42</sup> experimentally studied the addition of copper nanoparticles to alumina ( $\text{Al}_2\text{O}_3$ )/water nanofluid to measure the thermal conductivity of the final mixture. They observed that increasing the nanoparticle volume fraction resulted in an increase in both the viscosity and the thermal conductivity of the mixture. Takabi and Salehi<sup>46</sup> studied the natural convection within a corrugated enclosure heated on the bottom wall by a discrete heat source filled with a  $\text{Al}_2\text{O}_3$  – copper/water hybrid nanofluid. Chamkha, *et al.*<sup>47</sup> studied the unsteady conjugate natural convection within a semi-circular cavity using an  $\text{Al}_2\text{O}_3$  – Cu/water hybrid nanofluid, showing that the influence of the hybrid nanofluid was more effective at high Rayleigh numbers and thermal conductivity ratios (porous/fluid). Recently, Gorla, *et al.*<sup>48</sup>

reported the effects of a magnetic field on the natural convection inside a porous cavity filled with a hybrid nanofluid.

The majority of the previous literature has adopted the idea of local thermal equilibrium model (LTE) where the temperature of the solid (porous) phase is equal to the temperature of the fluid phase. However, it is important to note that the temperature of the solid phase is actually different to that of the fluid phase, which is referred to as the local thermal non-equilibrium (LTNE) model. This may be found in various engineering applications such as solar energy collectors and in the cooling of electronic components <sup>49</sup>. Several important studies <sup>50-54</sup> have investigated natural convection within enclosures entirely filled with porous media saturated with pure fluids under different boundary conditions using the LTNE model. Wu, *et al.*<sup>54</sup> studied the effects of sinusoidal and partially heated vertical sidewalls on the natural convection in a porous cavity saturated with a pure fluid using a numerical LTNE model. They concluded that the temperature convergence of the solid and the fluid phases was satisfied by increasing the interphase heat transfer coefficient ( $H$ ) and the fluid/solid thermal conductivity ratio ( $\gamma$ ). Natural convection inside an enclosure entirely filled with a porous medium saturated with a nanofluid has been investigated using the LTNE model in <sup>55-60</sup>. Sheremet and Pop<sup>60</sup> studied the natural convection in a tilted porous cavity saturated with a nanofluid according to the effects of the heater size and its position at the cavity wall using the LTNE model, observing that the heat transfer could be improved by reducing the distance between the position of the heater and the cold vertical walls.

As motivated by the relevant literature, the aim of this study is to investigate the effects of an isoflux bottom-heating wall on the convective heat transfer within superposed porous-hybrid nanofluid layers using the LTNE model. To the best of our knowledge, no such an investigation has yet been reported in the literature as applied to the study of fluid flow and heat transfer rates in a composite enclosure under the effects of a bottom-heated wall using the hybrid nanofluid and LTNE model. Therefore, in our opinion, this study should make an original contribution to this significant scientific field.

## II. MATHEMATICAL MODEL

The domain of this study is illustrated in FIG. 1 as that of a two-dimensional square enclosure with side length  $L$  composed of superposed porous-hybrid nanofluid layers. The bottom wall was partly heated using a heat flux of length  $b$  with a fixed centre location at a distance  $d$  from

the vertical wall. The inactive portion of the bottom wall was thermally insulated, while the upper and vertical walls were maintained at a constant cooled temperature,  $T_c$ . The Darcy-Brinkman model was used to model the flow in the porous medium layer, whilst the effects of the Forchheimer model were neglected. The hybrid nanofluid, composed of Cu – Al<sub>2</sub>O<sub>3</sub>/ water, saturated the porous layer on the left and filled the fluid layer on the right. The hybrid nanofluid in this analysis was assumed to be a homogenous mixture and laminar and incompressible. The pure fluid and the nanoparticles were in thermal equilibrium. The thermophysical properties of the hybrid nanofluid are given in TABLE I, and were assumed constant except for density variations, which were determined based on the Boussinesq approximation.

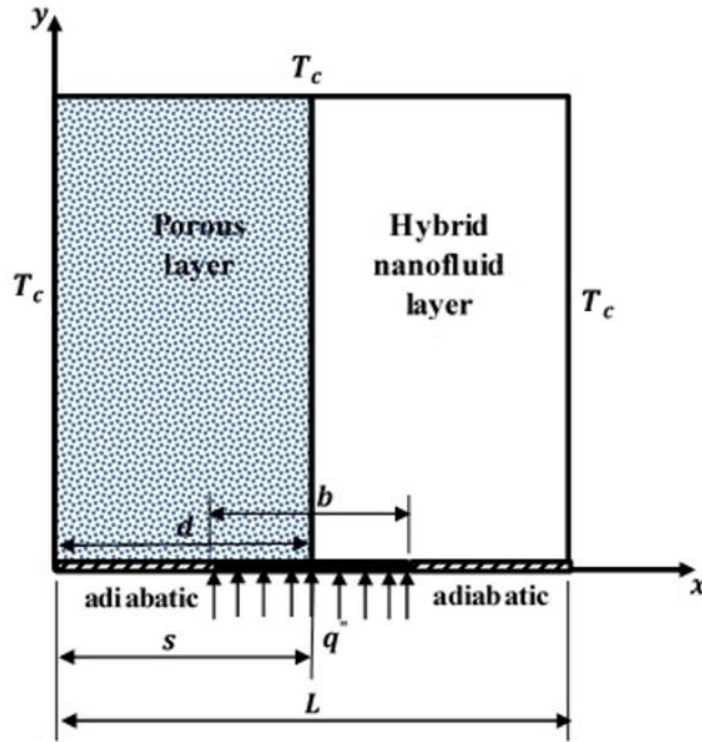


FIG. 1: Physical domain of composite hybrid nanofluid-porous medium layers.

TABLE I. Thermophysical properties of water, copper, and alumina<sup>48</sup>.

Property	Water	Copper (Cu)	Alumina (Al <sub>2</sub> O <sub>3</sub> )
$\rho$ (kg/m <sup>3</sup> )	997.1	8933	3970
$C_p$ (J/kg.K)	4179	385	765
$k$ (W/m.K)	0.613	401	40
$\beta$ (1/K)	$21 \times 10^{-5}$	$1.67 \times 10^{-5}$	$0.85 \times 10^{-5}$

## A. Dimensionless forms of equations

In the present study, the porosity value ( $\epsilon$ ) of the porous layer was assumed to be 1 and the effects of the permeability value ( $K$ ) in the Darcy number were adopted. According to these assumptions, and depending on the governing equations given by 35, the mass, momentum, and conservation of energy equations of the hybrid nanofluid-porous layers, including the non-equilibrium model relation presented in 58, are given in the following

Fluid layer

$$\frac{\partial(U)_{hnf}}{\partial X} + \frac{\partial(V)_{hnf}}{\partial Y} = 0 \quad (1)$$

$$(U)_{hnf} \frac{\partial(U)_{hnf}}{\partial X} + (V)_{hnf} \frac{\partial(U)_{hnf}}{\partial Y} = -\frac{\partial P}{\partial X} + \frac{(\rho)_{bf}}{(\rho)_{hnf} \times (1-\phi)^{2.5}} \times Pr \times \left( \frac{\partial^2(U)_{hnf}}{\partial X^2} + \frac{\partial^2(U)_{hnf}}{\partial Y^2} \right) \quad (2)$$

$$(U)_{hnf} \frac{\partial(V)_{hnf}}{\partial X} + (V)_{hnf} \frac{\partial(V)_{hnf}}{\partial Y} = -\frac{\partial P}{\partial Y} + \frac{(\rho)_{bf}}{(\rho)_{hnf} \times (1-\phi)^{2.5}} \times Pr \times \left( \frac{\partial^2(V)_{hnf}}{\partial X^2} + \frac{\partial^2(V)_{hnf}}{\partial Y^2} \right) + \frac{(\rho\beta)_{hnf}}{(\rho)_{hnf} \times (\beta)_{bf}} \times Pr \cdot Ra \cdot (\theta)_{hnf} \quad (3)$$

$$(U)_{hnf} \frac{\partial(\theta)_{hnf}}{\partial X} + (V)_{hnf} \frac{\partial(\theta)_{hnf}}{\partial Y} = \left( \frac{(\alpha)_{hnf}}{(\alpha)_{bf}} \right) \times \left[ \left( \frac{\partial^2 \theta_{hnf}}{\partial X^2} + \frac{\partial^2 \theta_{hnf}}{\partial Y^2} \right) + H * ((\theta)_{hnf} - (\theta)_p) \right] \quad (4)$$

Porous/Fluid layer

$$\frac{\partial(U)_{hnf}}{\partial X} + \frac{\partial(V)_{hnf}}{\partial Y} = 0 \quad (5)$$

$$(U)_{hnf} \frac{\partial(U)_{hnf}}{\partial X} + V_{hnf} \frac{\partial(U)_{hnf}}{\partial Y} = -\frac{\partial P}{\partial X} + \frac{(\rho)_{bf}}{(\rho)_{hnf} \times (1-\phi)^{2.5}} \times Pr \left( \frac{\partial^2(U)_{hnf}}{\partial X^2} + \frac{\partial^2(U)_{hnf}}{\partial Y^2} \right) - \frac{(\rho)_{bf}}{(\rho)_{hnf} \times (1-\phi)^{2.5}} \times \frac{Pr}{Da} \times (U)_{hnf} \quad (6)$$

$$(U)_{hnf} \frac{\partial(V)_{hnf}}{\partial X} + (V)_{hnf} \frac{\partial(V)_{hnf}}{\partial Y} = -\frac{\partial P}{\partial Y} + \frac{(\rho)_{bf}}{(\rho)_{hnf} \times (1-\phi)^{2.5}} \times Pr \left( \frac{\partial^2(V)_{hnf}}{\partial X^2} + \frac{\partial^2(V)_{hnf}}{\partial Y^2} \right) + \frac{(\rho \times \beta)_{hnf}}{(\rho)_{hnf} \times (\beta)_{bf}} \times Pr.Ra.(\theta)_{hnf} - \frac{(\rho)_{bf}}{(\rho)_{hnf} \times (1-\phi)^{2.5}} \times \frac{Pr}{Da} (V)_{hnf} \quad (7)$$

$$(U)_{hnf} \frac{\partial(\theta)_{hnf}}{\partial X} + (V)_{hnf} \frac{\partial(\theta)_{hnf}}{\partial Y} = \left( \frac{(\alpha)_{hnf}}{(\alpha)_{bf}} \right) * \left[ \left( \frac{\partial^2(\theta)_{hnf}}{\partial X^2} + \frac{\partial^2(\theta)_{hnf}}{\partial Y^2} \right) + H * ((\theta)_p - (\theta)_{hnf}) \right] \quad (8)$$

$$\frac{\partial(\theta)_{hnf}}{\partial X} + \frac{\partial(\theta)_{hnf}}{\partial Y} = \gamma * H * [(\theta)_p - (\theta)_{hnf}] \quad (9)$$

Theses governing equations are performed based on the dimensionless transform parameters as follows

$$X = \frac{x}{L}, Y = \frac{y}{L}, U = \frac{u \times L}{(\alpha)_{bf}}, V = \frac{v \times L}{(\alpha)_{bf}}, P = \frac{P \times L}{(\rho)_{hnf} (\alpha)_{bf}^2}, \Delta T = \frac{q'' \times L}{(k)_{bf}},$$

$$(\theta)_{hnf} = \frac{(T)_{hnf} - (T)_c}{(T)_w - (T)_c}, (\theta)_p = \frac{(T)_p - (T)_c}{(T)_w - (T)_c}, Ra = \frac{(\beta)_{bf} \times g \times \Delta T \times L^3}{(\rho)_{bf} \times (\alpha)_{bf}}, Pr = \frac{(\rho)_{bf}}{(\rho)_{hnf}}, Da = \frac{K}{L^2}, \gamma = \frac{(k)_{hnf}}{(k)_p}, H = \frac{h \times L^2}{(k)_{hnf}}. \quad (10)$$

The stream function intensity and the direction of the streamlines can be simulated using the following equation, where the positive sign of  $\Psi$  refers to an anticlockwise flow direction, and a negative sign indicates a clockwise flow direction.

$$\frac{\partial^2 \Psi}{\partial X^2} + \frac{\partial^2 \Psi}{\partial Y^2} = \frac{\partial U}{\partial Y} - \frac{\partial V}{\partial X} \quad (11)$$

The heat conduction is equal to the heat convection and to satisfy the dimensionless heat flux parameter,  $\frac{\partial(\theta)}{\partial(x)}$  should be equal to  $\frac{(k)_{bf}}{(k)_{hnf}}$  as follows<sup>61</sup>

$$q'' = \frac{(k)_{hnf}}{(k)_{bf}} \times \frac{\partial(\theta)}{\partial(x)} = h \times (\theta)_w$$

therefore,

$$(12)$$

$$h = \frac{1}{(\theta)_w}$$

$h$  represents the heat transfer coefficient and  $(\theta)_w$  represents the dimensionless wall temperature distribution along the heat source. The local and average Nusselt number expressions along the heat source length thus become

$$Nul(X) = \frac{[h \times L]}{\left( \frac{(k)_{hnf}}{(k)_{bf}} \right)} \quad (13)$$

$$Nu_{av} = \frac{1}{B} \int_{D-0.5B}^{D+0.5B} Nul(X) dX \quad (14)$$

## B. Thermo-physical properties of the hybrid nanofluid

The physical property equations for the Cu – Al<sub>2</sub>O<sub>3</sub>/water hybrid nanofluid are simulated with a nanoparticle volume fraction,  $\phi$ , depending on the physical properties of the nanofluid equations presented in the reference 48.

$$\rho_{hnf} = [(\phi)_{Cu} \times (\rho)_{Cu} + (\phi)_{Al_2O_3} \times (\rho)_{Al_2O_3}] + (1 - \phi) \times (\rho)_{bf} \quad (15)$$

$$(\mu)_{hnf} = \frac{(\mu)_{bf}}{[1 - ((\phi)_{Cu} + (\phi)_{Al_2O_3})]^{2.5}} \quad (16)$$

$$(\rho \times Cp)_{hnf} = [(\phi)_{Cu} \times (\rho \times Cp)_{Cu} + (\phi)_{Al_2O_3} \times (\rho \times Cp)_{Al_2O_3}] + (1 - \phi) \times (\rho \times Cp)_{bf} \quad (17)$$

$$(\rho \times \beta)_{hnf} = [(\phi)_{Cu} \times (\rho \times \beta)_{Cu} + (\phi)_{Al_2O_3} \times (\rho \times \beta)_{Al_2O_3}] + (1 - \phi) \times (\rho \times \beta)_{bf} \quad (18)$$

$$(\alpha)_{hnf} = \frac{(k)_{hnf}}{(\rho \times Cp)_{hnf}} \quad (19)$$



$$\begin{aligned}
(k)_{hnf} = & \left\{ \left[ \frac{[(\phi)_{Cu} \times (k)_{Cu} + (\phi)_{Al_2O_3} \times (k)_{Al_2O_3}]}{\phi} + 2 \times (k)_{bf} + 2 \times [(\phi)_{Cu} \times \right. \right. \\
& (k)_{Cu} + (\phi)_{Al_2O_3} \times (k)_{Al_2O_3}] - 2 \times \phi \times (k)_{bf} \Big] \times \\
& \left[ \frac{[(\phi)_{Cu} \times (k)_{Cu} + (\phi)_{Al_2O_3} \times (k)_{Al_2O_3}]}{\phi} + 2 \times (k)_{bf} - [(\phi)_{Cu} \times \right. \\
& (k)_{Cu} + (\phi)_{Al_2O_3} \times (k)_{Al_2O_3}] + (\phi) \times (k)_{bf} \Big]^{-1} \Big\} \times (k)_{bf}
\end{aligned} \tag{20}$$

### C. Boundary conditions

The boundary conditions for the selected domain are:

$$U(X, 0) = U(X, 1) = U(0, Y) = U(1, Y) = 0,$$

$$V(X, 0) = V(X, 1) = V(0, Y) = V(1, Y) = 0,$$

$$\theta(X, 1) = \theta(0, Y) = \theta(1, Y) = 0,$$

$$\frac{\partial \theta}{\partial Y}(X, 0) = -\frac{k_{bf}}{k_{hnf}}, \quad (D - 0.5B) \leq X \leq (D + 0.5B)$$

$$\frac{\partial \theta}{\partial Y}(X, 0) = 0, \quad 0 \leq X < (D - 0.5B) \text{ and } (D + 0.5B) < X \leq 1 \tag{21}$$

The boundary conditions at the interface between the porous and fluid layers are permeable when the values of the tangential and normal velocities, the shear and normal stresses, and the temperature and heat flux are equal.

### III. NUMERICAL SOLUTION AND VALIDATION

The numerical algorithm was used to solve the dimensionless governing Eqs. (1)–(9) with the boundary conditions in Eq. (21) via the Galerkin finite element methodology, using the Computational Fluid Dynamics (CFD) solver available in the Multiphysics COMSOL 5.1 software suite. The non-linear equations were transformed to linear equations based on the basis set employed, the method for which is described in detail in reference 62. The coefficients of the linear residual equations were estimated using the Newton-Raphson method. The SIMPLE algorithm was used to satisfy the coupling between the continuity and momentum

equations. The solution convergence was dependent on the criteria of the dependent variables reaching steady-state values and satisfying the following relation:

$$\frac{\sum_{i=1}^m \sum_{j=1}^n |\Phi_{i,j}^{r+1} - \Phi_{i,j}^r|}{\sum_{i=1}^m \sum_{j=1}^n |\Phi_{i,j}^{r+1}|} \leq 10^{-6} \quad (22)$$

where  $\Phi$  represents the dimensionless parameters of the velocity components ( $U$ ,  $V$ ), temperature  $\theta$ , or the pressure  $P$  of the domain. The subscript terms  $i$  and  $j$  indicate the  $i^{th}$  and  $j^{th}$  grid in the  $x$  and  $y$  directions, respectively. The superscript  $r$  indicates the  $r^{th}$  iteration.  $m$  and  $n$  refer to the total number of nodes.

Several independent grid tests were performed with element numbers of  $30 \times 30$ ,  $40 \times 40$ ,  $60 \times 60$ ,  $80 \times 80$ ,  $100 \times 100$ ,  $110 \times 110$ ,  $120 \times 120$ ,  $130 \times 130$ ,  $140 \times 140$  and  $160 \times 160$  to determine the proper grid size of this study. Figure 2 illustrates the average Nusselt numbers calculated at different grid sizes for an enclosure that was partly filled with a hybrid nanofluid and also partly filled with a porous layer saturated with the same type of nanofluid at  $Ra = 10^7$ ,  $Da = 10^{-3}$ ,  $\phi = 0.2$ ,  $B = 0.4$ ,  $D = S = 0.5$ ,  $\gamma = 10$  and  $H = 50$ . A  $130 \times 130$  grid was used to assess the accuracy of the numerical procedure because this was found to give an almost constant solution to the converged value of the average Nusselt number. The validation tests for the present solver were satisfied with previously published studies for different cases. The validation results compared with the results presented by Aminossadati and Ghasemi<sup>61</sup> for the streamlines and isotherm contours at  $Ra = 10^5$ ,  $B = 0.4$ ,  $D = 0.5$  and  $\phi = 0.1$ , as shown in FIG.3. In addition, Table II compares the average Nusselt number on the heat source wall for

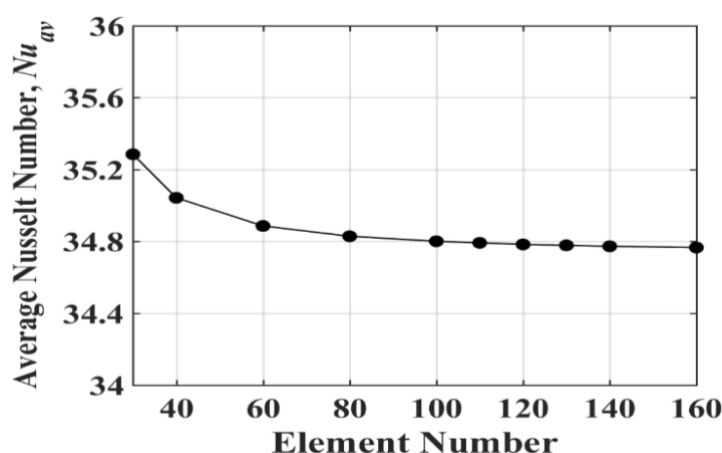


FIG. 2. Grid testing for the average Nusselt number at different element numbers.

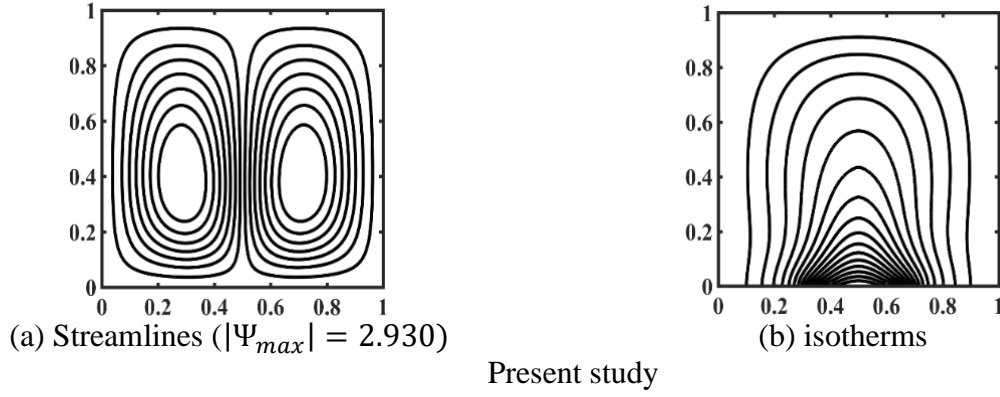


FIG. 3 Streamlines (a) and isotherms (b) of the present study are in agreement with those of benchmark problem of Aminossadati and Ghasemi<sup>61</sup> at  $Ra = 10^5$ ,  $B = 0.4$ ,  $D = 0.5$  and  $\phi = 0.1$ . different Rayleigh numbers, where an acceptably small difference was found between the selected and the present studies. To increase confidence in the results produced by the selected solver, FIG.4 shows a further validation of the results presented by Baytas<sup>51</sup> for the natural convection inside a porous enclosure with heat generated using the thermal nonequilibrium model. The validation of the temperature profile was examined for the Brinkman-Darcy-Forchheimer model at  $X = 0.5$  when  $Ra = 10^7$ ,  $Da = 10^{-2}$ ,  $\varepsilon = 0.4$ ,  $Pr = 7$ ,  $F_0 = 5.648$ ,  $\gamma = 0.1$ , and  $H = 1000$ . To validate the hybrid nanofluid case, FIG.5 shows the validation of the results presented by Gorla, *et al.*<sup>48</sup> for a porous enclosure saturated with a hybrid nanofluid that was differentially heated and cooled using two heat sources and sinks, respectively. The comparison of the results showed good agreement between our results and those reported in the literature, giving confidence as to the accuracy of the finite element solver selected.

TABLE II. Comparison of average Nussle number values on the bottom heat source wall of the cavity with the presented study by Aminossadati and Ghasemi<sup>61</sup>.

$Ra$	Aminossadati and Ghasemi <sup>61</sup>	Present study	Deviation %
$10^3$	5.451	5.566	2.11
$10^4$	5.474	5.588	2.08
$10^5$	7.121	7.218	1.36
$10^6$	13.864	14.018	1.11

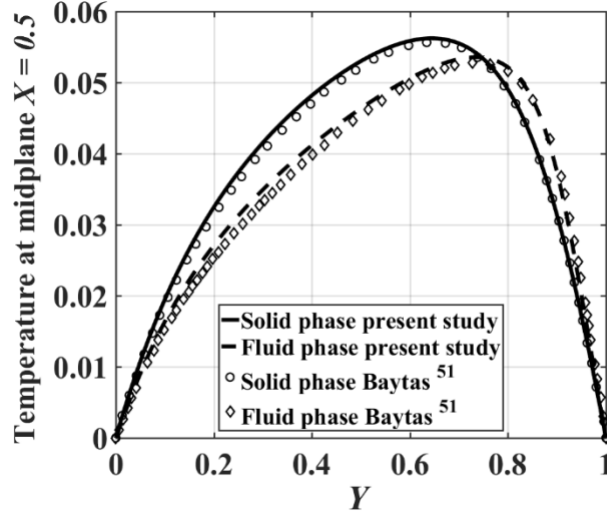


FIG. 4. Temperature profile at vertical midplane ( $X = 0.5$ ) with  $Ra = 10^7$ ,  $Da = 10^{-2}$ ,  $\varepsilon = 0.4$ ,  $Pr = 7$ ,  $F_0 = 5.648$ ,  $\gamma = 0.1$ , and  $H = 1000$ . The symbols correspond to Baytas<sup>51</sup> and the lines correspond to the present study.

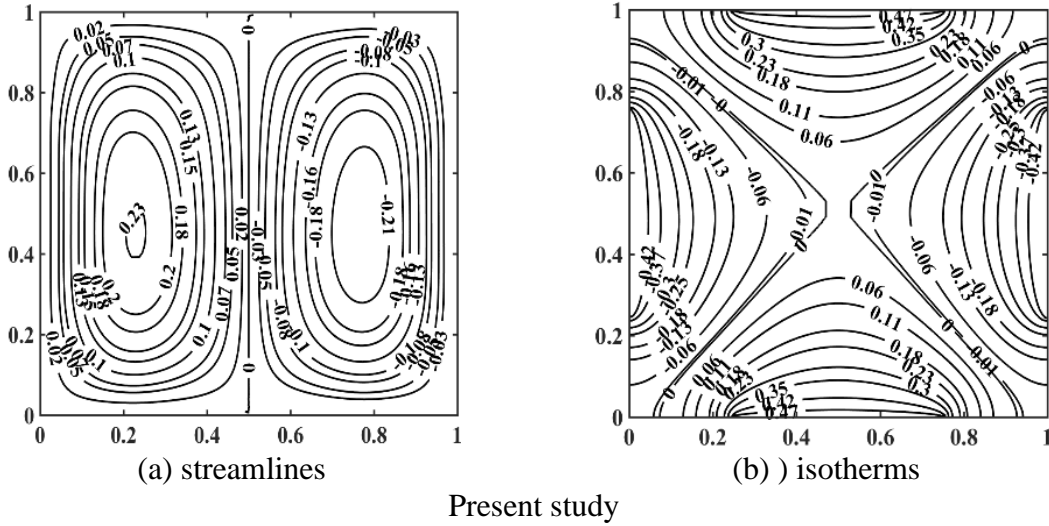


FIG. 5. Streamlines (a) and isotherms (b) of the present study are in agreement with those of benchmark problem of Gorla, *et al.*<sup>48</sup> at  $Ra = 10^4$ ,  $Da = 10^{-3}$ , Hartman number = 0,  $D = B = 0.5$  and  $\phi = 0.05$ .

#### IV. RESULTS AND DISCUSSION

In this section, the results of numerical simulations were determined for the streamline and isotherm contours and as graphical profiles of the resultant velocity and temperature distributions along the interface section between the hybrid nanofluid and porous layers within the cavity. In addition, the local and average Nusselt numbers were plotted against various selected effective parameters. In all figures of isotherm lines, the temperature distribution was at a maximum at the bottom-heated wall and at their minimum values at the upper horizontal

and vertical cold walls. The results were calculated for a Rayleigh number ( $Ra$ ) range of  $10^3 \leq Ra \leq 10^7$ . The Darcy number ( $Da$ ) was varied over the range  $10^{-7}$  to 1. The porous layer thickness ( $S$ ) was selected to lie within the range 0 – 1, whilst the modified conductivity ratio ( $\gamma$ ) was varied between  $10^{-1}$  and  $10^4$  and the interphase heat transfer coefficient ( $H$ ) range was  $10^{-1} \leq H \leq 1000$ . The choice of the heat source length ( $B$ ) was parameterized as 0.2, 0.4, 0.6, 0.8 and 1, and was located at the bottom wall at a fixed location from the sidewalls of  $D = 0.5$ . The selected nanoparticle volume fraction was set between  $\phi = 0 - 0.2$ , with equal percentages of each of the selected nanoparticle types. A detailed discussion of the effects of the selected parameters on the flow and heat transfer behaviour inside the chosen enclosure is presented in sections IV A-IV D.

## A. Streamlines and isotherms

The effect of varying the Rayleigh number ( $Ra$ ) on the contour maps for the streamlines (a), the fluid phase isotherms (b), and the solid phase isotherms (c) respectively, at  $Da = 10^{-3}$ ,  $B = 0.4$ ,  $S = D = 0.5$ ,  $\gamma = 10$  and  $H = 1$  is illustrated in FIG. 6. At low values of the Rayleigh number ( $Ra = 10^4$  and  $10^5$ ) as shown in FIG. 6(a), due to the boundary conditions being applied, the fluid near the heat source rose along the interface line in the fluid and porous layers due to the density variation. The fluid moved towards the upper cold wall at different velocities due to the resistance offered by the porous layer to the flow inside it. Thereafter, the flow descends along the left and right cooled walls in the porous and fluid layers. This was found to generate a relatively strong main vortex with a clockwise flow direction, which effectively covered the fluid layer, and a weak secondary vortex with an anticlockwise flow direction in the porous layer. The pole centres of the vortices were located near the bottom-heated wall. As the Rayleigh number was increased to  $10^6$ , the vortex of the fluid layer tended to compress the vortex in the porous layer and force it away from the interface line, with associated substantial intensity changes in the stream function values compared to the lower Rayleigh numbers. The addition of a 20% hybrid nanofluid resulted in a decrease in the strength of the flow (see  $\Psi_{min}$  values). This was attributed to the effects of the viscous force being greater than those of the inertial force. A higher Rayleigh number causes the vortex of the hybrid nanofluid in the porous layer tries to compress the vortex in the fluid layer as compared to the vortices found for the pure fluid. This behaviour was found to occur at a greater strength of stream function in the porous layer compared to other Rayleigh number values, where the inertial force overcame the viscous force. The core centre of the hybrid nanofluid vortex in the fluid layer was closer to

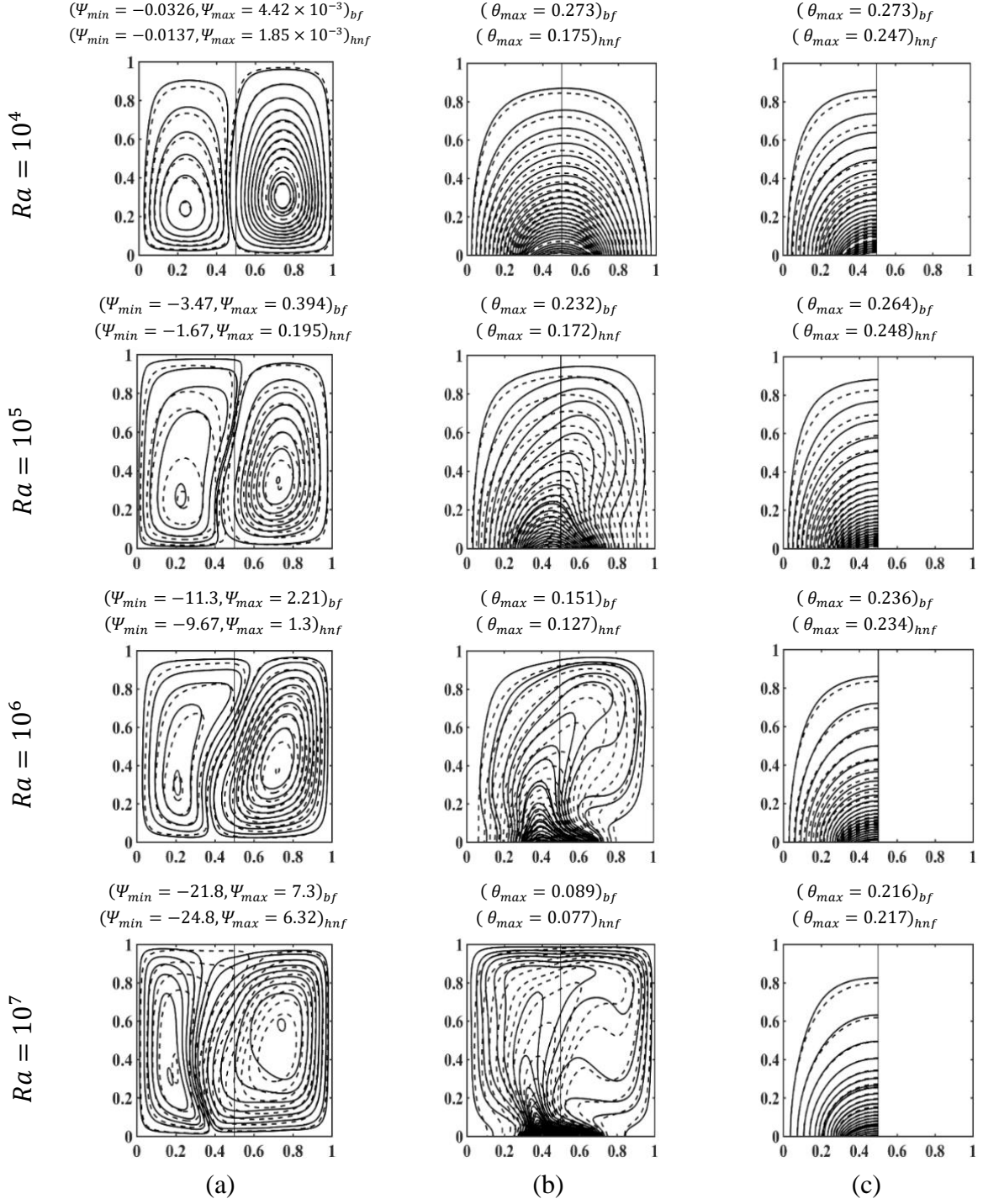


FIG. 6. Contour maps of (a) the streamlines, (b) the fluid phase isotherms  $(\theta_{max})_f$ , and (c) the solid phase isotherms  $(\theta_{max})_p$  for different Rayleigh numbers, using  $Da = 10^{-3}$ ,  $S = 0.5$ ,  $B = 0.4$ ,  $D = 0.5$ ,  $\gamma = 10$ ,  $H = 1$ ,  $\phi = 0$  (solid lines) and  $\phi = 0.2$  (dashed lines).

the bottom heat source than the core centre of the pure fluid vortex, which resulted in a greater increase in the intensity of the streamlines of the hybrid nanofluid than that was found for the pure fluid. FIG. 6(b) shows a monotonical distribution of the isotherm lines in the fluid phase

was observed with lines parallel to the heat source, which showed a symmetrical pattern at a lower Rayleigh numbers. This behaviour was found to change, with a greater deformation of the isotherm lines with increasing the Rayleigh number. The behaviour of the isotherm lines showed that the plume of isotherm lines extending from the porous layer towards the fluid layer occurred with a significant reduction in the thickness of the thermal boundary layer at the heat source line and the vertical cooled walls. This was indicative of increasing heat transfer rates at higher Rayleigh numbers. The isotherm pattern for the solid phase (porous medium) had a uniform distribution, with an increased isotherm line density at the heat source with increasing Rayleigh number as shown in FIG. 6(c). The deviations in the temperature distributions between the pure fluid and the hybrid nanofluid decreased with increasing Rayleigh number, where the isotherm lines of the pure fluid tended to match those of the hybrid nanofluid. It is interesting to note that the presence of the nanoparticles worked to reduce the maximum temperature inside the enclosure, as seen from the  $\theta_{max}$  values for the fluid and solid phases. This was due to the significant increase in the streamlines strength and the thermal conductivity effects of the nanoparticles.

FIG. 7 shows the influence of the dimensionless permeability parameter (Darcy number,  $Da$ ) on the contour maps for the streamlines (a), the fluid phase isotherms (b), and the solid phase isotherms (c) respectively, for  $Ra = 10^6$ ,  $B = 0.4$ ,  $S = D = 0.5$ ,  $\gamma = 10$  and  $H = 1$ . FIG. 7(a) shows that at  $Da = 10^{-5}$ , two vortices in the pure fluid and one in the hybrid nanofluid were observed in the respective fluid layers. The primary vortex for both the pure fluid and hybrid nanofluid occupied most of the fluid layer and had a clockwise direction of motion, which was of greater strength than the secondary (anticlockwise) vortex for the pure fluid located in the upper left corner of the respective fluid layers. There was a very low penetration of the flow ( $Da = 10^{-5}$ ) for both the pure fluid and hybrid nanofluid into the porous layer due to the low permeability of the porous medium. Increasing the Darcy number to  $Da = 10^{-3}$  resulted in two larger vortices in both the porous and fluid layers compared to  $Da = 10^{-5}$ , as shown in FIG. 6(a) ( $Ra = 10^6$ ). As the Darcy number was increased, a relatively small increase in the stream function intensity was observed for the clockwise vortex in the hybrid nanofluid, while there was a relatively significant increase in the stream function for the anticlockwise vortex in the porous layer. This was due to the lower resistance offered by the porous layer when Darcy number was increased. The thermal distribution plumes for both the pure fluid and hybrid nanofluid in the fluid phase tended to move from the inclined direction in the fluid layer towards the vertical direction along the interface line, as shown in FIG. 7(b). This led to a

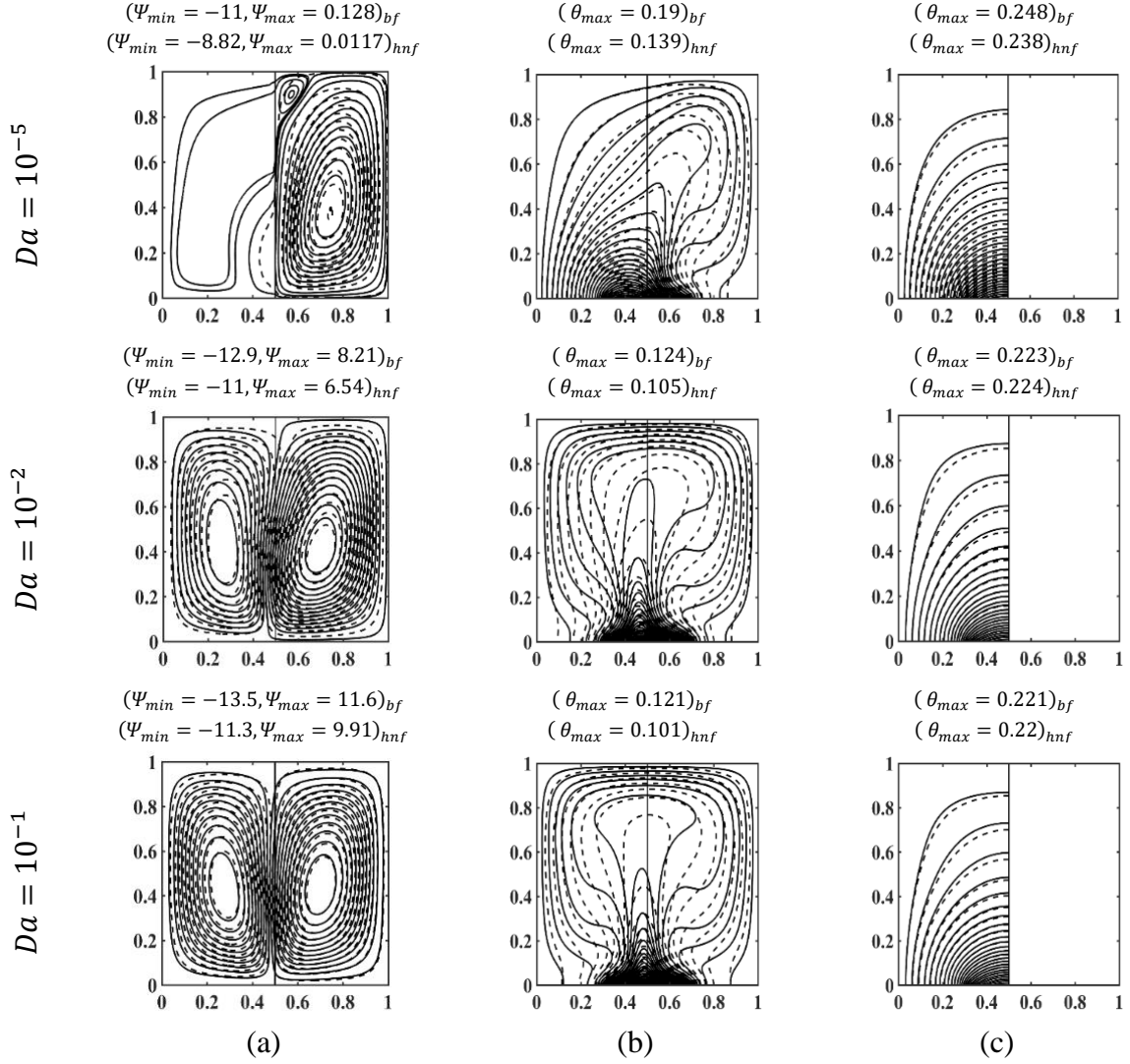


FIG. 7. Contour maps of (a) the streamlines, (b) the fluid phase isotherms  $(\theta_{max})_f$ , and (c) the solid phase isotherms  $(\theta_{max})_p$  for different Darcy numbers, using  $Ra = 10^6$ ,  $S = 0.5$ ,  $B = 0.4$ ,  $D = 0.5$ ,  $\gamma = 10$ ,  $H = 1$ ,  $\phi = 0$  (solid lines) and  $\phi = 0.2$  (dashed lines).

reduction in the thermal boundary layer thickness along the bottom-heated wall with a symmetrical distribution in the isotherm lines. This indicates improved heat transfer rates. FIG. 7(c) shows the isotherms for the solid phase seem to show a thinner thermal boundary layer as Darcy number increases with an increasing correspondence in the isotherms found in the pure fluid and nanofluid cases. The addition of a 20% nanoparticle sample causes the temperature inside the enclosure to decrease, as per the associated reduction in  $\theta_{max}$  values.

FIG. 8 illustrates the effect of the thickness of the porous layer on the contour maps of the streamlines (a), the fluid phase isotherms (b), and the solid phases isotherms (c) respectively, when  $Ra = 10^6$ ,  $Da = 10^{-3}$ ,  $B = 0.4$ ,  $D = 0.5$ ,  $\gamma = 10$  and  $H = 1$ . Two symmetrical vortices



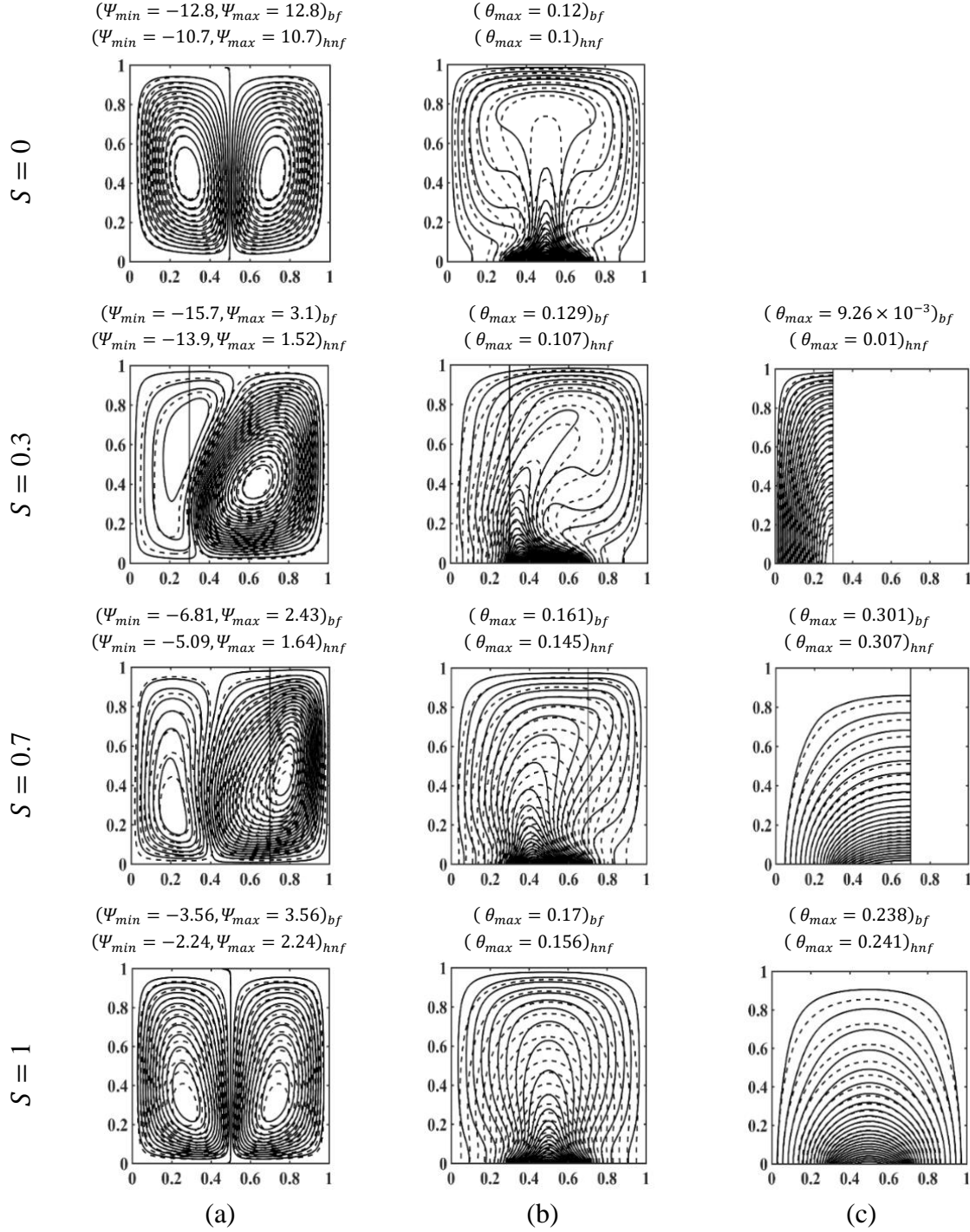


FIG. 8. Contour maps of (a) the streamlines, (b) the fluid phase isotherms  $(\theta_{max})_f$ , and (c) the solid phase isotherms  $(\theta_{max})_p$  for different porous layer thicknesses, using  $Ra = 10^6$ ,  $Da = 10^{-3}$ ,  $B = 0.4$ ,  $D = 0.5$ ,  $\gamma = 10$ ,  $H = 1$ ,  $\phi = 0$  (solid lines) and  $\phi = 0.2$  (dashed lines).

with elliptical shapes appear inside the enclosure with equal strengths in both the clockwise and anticlockwise flow directions for both the pure fluid and the hybrid nanofluid at  $S = 0$ , as shown in FIG. 8(a). This Figure also shows that at  $S = 0.3$ , asymmetric vortices appear inside the enclosure for both the pure fluid and the hybrid nanofluid cases because of the resistance of the porous layer to the flow inside it. The primary vortex occupies most of the fluid layer

and is semi-circular in shape with its centre located almost in the middle of the fluid layer; the secondary vortex centre is located close to the interface line at the upper part of the porous layer. A relative increase in the stream function strengths for this thickness in the porous layer was observed compared to  $S = 0$ . This was because the main vortex of the fluid layer effectively attached most of the heated source size, which caused to accelerate the flow. Increasing the porous layer thickness up to  $S = 1$  leads to a significant reduction in the stream function strength and the appearance of symmetrical vortices because of the equivalent effects of the porous medium on both vortices, which results in an increase in temperature inside the enclosure. FIG. 8(b) shows that the isotherms in the fluid phase is symmetrical at  $S = 0$ , where the plume of the isotherm lines is located at the vertical centreline of the enclosure. This pattern changes, with greater deformation of the isotherm lines for the fluid phase, with increasing porous layer thickness. At  $S = 1$ , a symmetric behaviour was observed in the isotherm lines with a reduction in the thickness of the thermal boundary layer and a significant increase in temperature inside the enclosure. The isotherms for the solid phase (porous medium) seem to have a uniform distribution with a lower temperature at  $S = 0.3$ , while the temperature reaches a maximum at  $S = 0.7$ , as shown in FIG. 8(c). The addition of a 20% sample of nanoparticles to the pure fluid results in a reduction in temperature inside the enclosure for the fluid phase. This is because of the increased thermal conductivity of the fluid, which results in greater cooling with the nanofluid than the pure fluid. Conversely, this addition causes an increase in the temperature of the solid phase due to an increase in the heat received by the porous medium from the heat source compared to the pure fluid, which leads to a more enhanced heat transfer. When the porous layer is not attached to any part of the heat source, this leads to the temperature of the fluid being greater than the solid phase, while if the porous layer is attached to either a part or the entirety of the heat source this leads to an increased temperature in the solid phase compared to the fluid phase. Generally, as expected when  $S = 0.3$ , the rate of heat transfer is enhanced compared to other porous layer thicknesses.

The effect of increasing the modified conductivity ratio from  $\gamma = 0.1$  to  $\gamma = 1000$  on the contour maps for the streamlines (a), the fluid phase isotherms (b), and the solid phase isotherms (c), for  $Ra = 10^4$ ,  $Da = 10^{-3}$ ,  $S = D = 0.5$  and  $H = 1$ . At  $\gamma = 0.1$  is illustrated in FIG. 9. FIG. 9(a) shows that the behaviour of the flow within the enclosure was evident from the two circulatory vortices produced. There is a significant deviation of the streamlines of the secondary vortices in the porous layer between the hybrid nanofluid and the pure fluid, which are of lower intensities compared to the vortices located in the fluid layer. Increasing the modified thermal

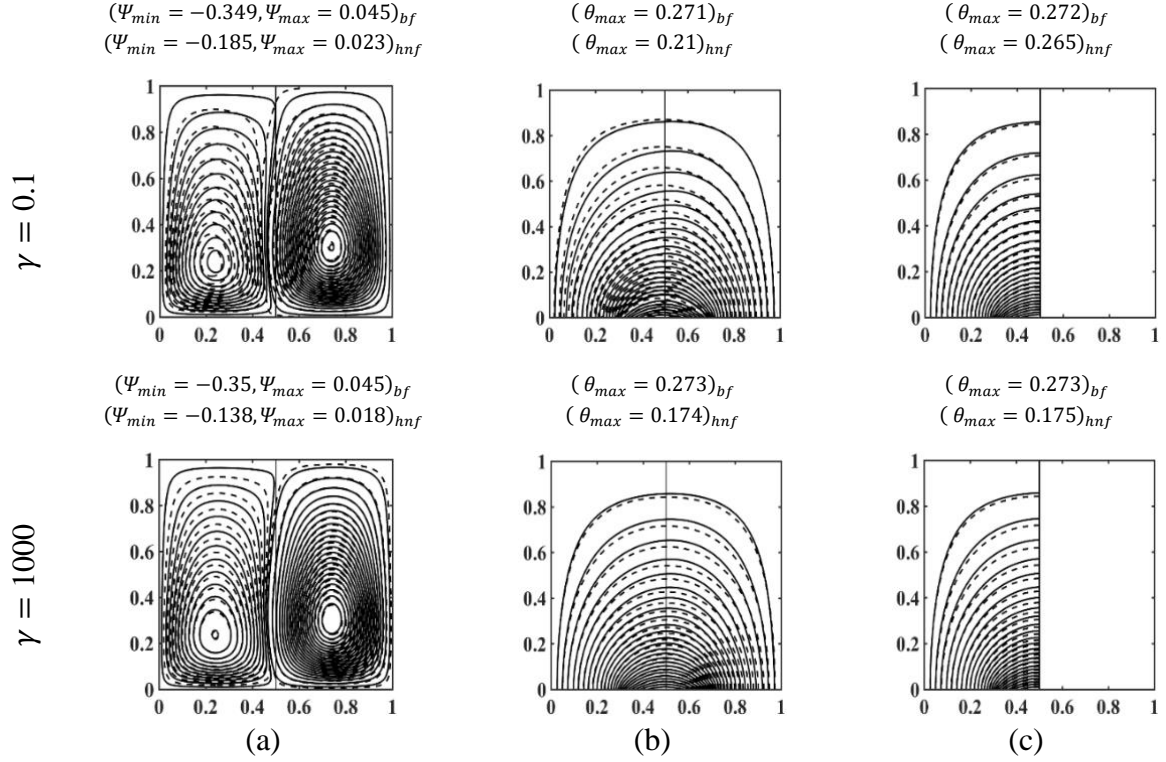


FIG. 9. Contour maps of (a) the streamlines, (b) the fluid phase isotherms  $(\theta_{max})_f$ , and (c) the solid phase isotherms  $(\theta_{max})_p$  for various modified conductivity ratios, using  $Ra = 10^4$ ,  $Da = 10^{-3}$ ,  $S = 0.5$ ,  $B = 0.4$ ,  $D = 0.5$ ,  $H = 50$ ,  $\phi = 0$  (solid lines) and  $\phi = 0.2$  (dashed lines).

conductivity ratio to 1000 led to that the streamfunction strength of the hybrid nanofluid vortices appears more sensitive to an increased thermal conductivity ratio than that of the pure fluid, while there are no effects on the stream function values in the instance of the pure fluid.

The hybrid nanofluid vortex was found to move towards the left cooled wall. This resulted in a deviation of the isotherm lines in the porous layer between the hybrid nanofluid and the pure fluid more than that of the deviation at the fluid layer, as shown in FIG. 9(b). FIG. 9(c) observes the isotherm patterns within the solid phase appear essentially identical for both the pure fluid and hybrid nanofluid. A convergence of the temperature distributions occurred in the fluid and solid phases to near identity. This leads to thermal equilibria with similar isotherm patterns and magnitudes in the fluid and porous phases, which is representative of the ideal heat exchange between the fluid and porous phases with a greater enhancement of the heat transfer.

FIG. 10 shows the effects of increasing the length of the heat source on the contour maps for the streamlines (a), the fluid phase isotherms (b), and the solid phase isotherms (c) at  $Ra = 10^6$ ,  $Da = 10^{-3}$ ,  $S = D = 0.5$ ,  $\gamma = 10$  and  $H = 1$ . FIG. 10(a) shows that when the length of

the heat source is increased, two asymmetrical counter-rotating vortices of different streamline densities and stream function strengths are created due to the resistance offered by the porous layer. In addition, increasing the length of the heat source leads to an increase in temperature

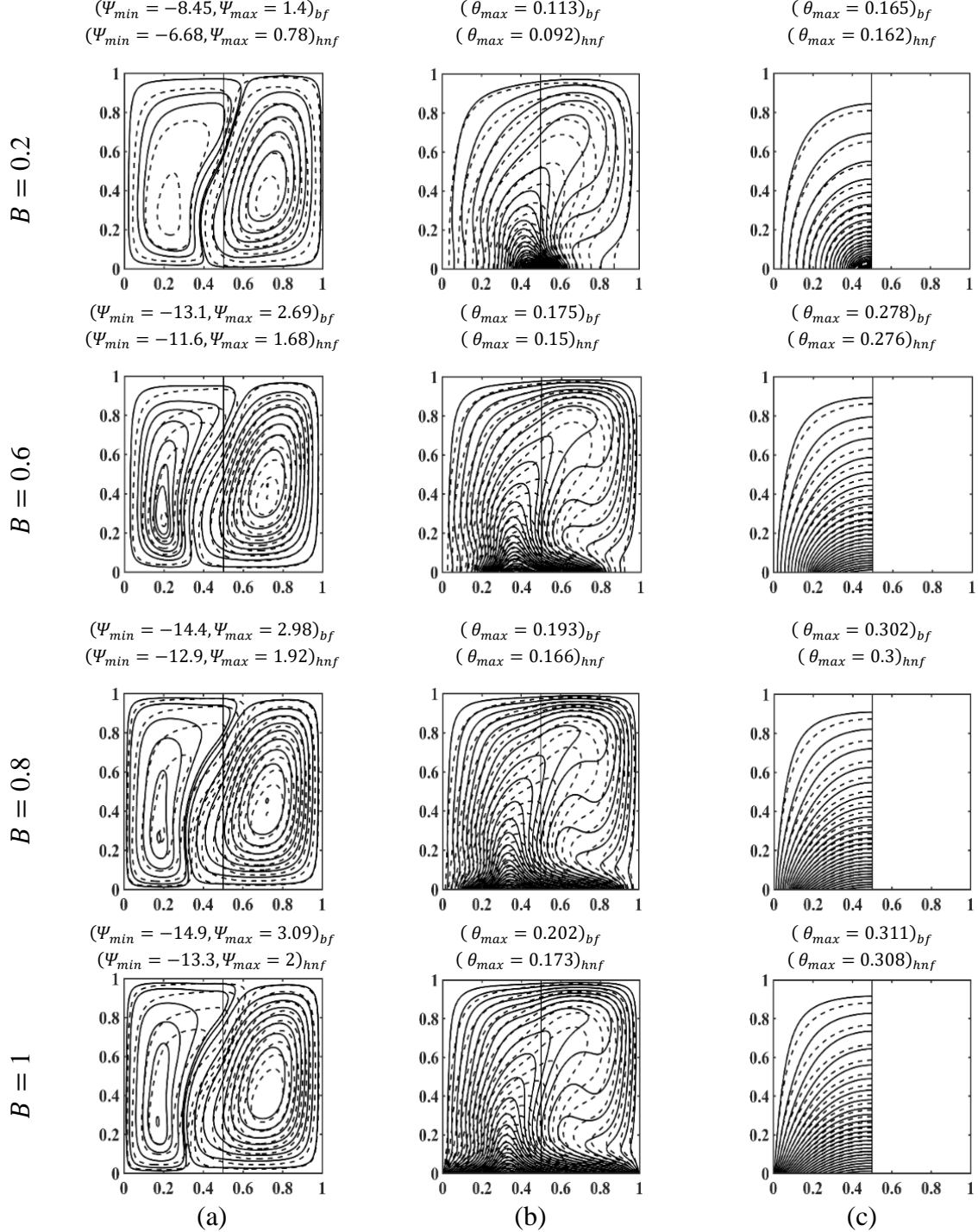


FIG. 10. Contour maps of (a) the streamlines, (b) the fluid phase isotherms  $(\theta_{max})_f$ , and (c) the solid phase isotherms  $(\theta_{max})_p$  for different bottom-heated wall lengths, using  $Ra = 10^6$ ,  $Da = 10^{-3}$ ,  $S = 0.5$ ,  $D = 0.5$ ,  $\gamma = 10$ ,  $H = 1$ ,  $\phi = 0$  (solid lines) and  $\phi = 0.2$  (dashed lines).

within the fluid and porous phases as shown in FIG. 10(b) and (c), respectively. This was due to the large amount of heat generated, which led in turn to an increase in buoyancy force. It is interesting to note that increasing the length of heat source reduces the thickness of the thermal boundary layer, with a greater isotherm density close to the hot and cold walls, especially in the fluid layer.

## B. Velocity resultant, $R$ , and temperature difference distributions

To gain a better understanding of the flow and thermal behaviour in this situation, the dimensionless resultant velocity with various (a) Rayleigh numbers and (b) modified thermal conductivities along the interface line between the porous and fluid layers at  $X = 0.5$  are presented in FIG. 11. FIG. 11(a) depicts the variation in the resultant velocities for different Rayleigh numbers at  $Da = 10^{-3}$ ,  $B = 0.4$ ,  $S = D = 0.5$ ,  $\gamma = 10$  and  $H = 50$ . Increasing the Rayleigh number increased the resultant velocity value because of the increased buoyancy. Oscillation of resultant velocity pattern occurs inside the cavity, and this oscillation increases with increasing Rayleigh number. This is due to the interaction of the two counter-rotating vortices that occurred in the hybrid nanofluid within the enclosure. FIG. 11(b) shows the effects of the modified thermal conductivity ratio on the resultant velocity at  $Ra = 10^6$ ,  $Da = 10^{-3}$ ,  $B = 0.4$ ,  $S = D = 0.5$  and  $H = 50$ . Decreasing the modified thermal conductivity ratio led to an increase in the resultant velocity due to ability of the porous medium to receive heat from the heat source.

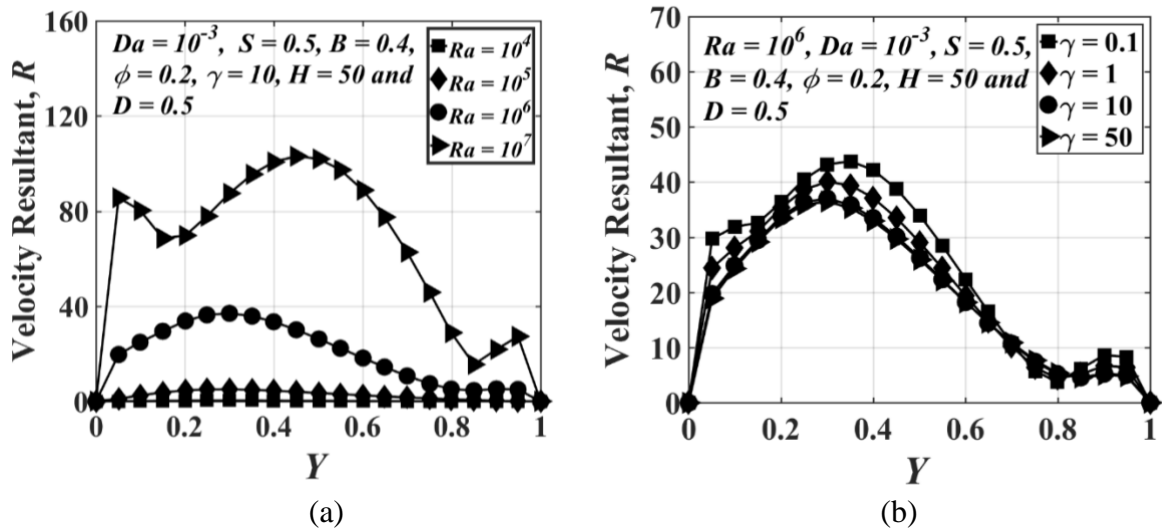


FIG. 11. Variation of velocity resultant at the interface vertical mid-plane of the domain ( $X = 0.5$ ) for different values of (a) Rayleigh number (b) thermal conductivity ratio.

Figure 12 shows the temperature difference between the solid and hybrid nanofluid phases with different (a) Rayleigh numbers and (b) modified thermal conductivities along the interface line between the porous and fluid layers at  $X = 0.5$ , as shown in FIG.12(a) and (b), respectively. The maximum temperature difference between the solid and the hybrid nanofluid phases occurs at  $Y = 0$ , while the minimum difference occurs at the upper wall of the enclosure with different Rayleigh numbers as shown in FIG.12(a). The temperature difference decreases with decreasing the Rayleigh number. This means at lower Rayleigh numbers ( $Ra \leq 10^5$ ), the temperature of the solid phase (porous medium) is similar to the temperature of the hybrid nanofluid phase. This leads to thermal equilibrium, indicative of a high heat transfer rate between the solid and nanofluid phases. Increasing  $Ra$  results in an increase in the temperature difference between the solid and the hybrid nanofluid phases. Increasing the modified thermal conductivity leads to a reduction the temperature difference that ultimately reaches zero - that is, thermal equilibrium - as shown in FIG. 12(b). Generally, for a high Rayleigh number and low modified thermal conductivity ratio, especially at  $Ra > 10^5$  and  $\gamma < 1$ , the variation in the temperature difference between the solid and hybrid nanofluid phases would take negative and positive values in the upper and lower parts of the enclosure, respectively.

Figure 13 shows the dimensionless temperature distribution along the heat source with increasing porous layer thickness for two different Rayleigh numbers, (a)  $Ra = 10^4$  and (b)  $Ra = 10^7$  at  $Da = 10^{-3}$ ,  $B = 0.4$ ,  $D = 0.5$ ,  $\gamma = 10$  and  $H = 50$ . Figure 13(a) illustrates that the temperature distribution seems to be symmetric along the heat source with a maximum value at its centre. Increasing the porous layer thickness from 0.0 to 0.3 leads to a reduction in the heat source temperature, which indicates increased cooling of the heat source wall. However, it was found that increasing the thickness of the porous layer to a higher value than 0.3 increased the temperature of the heat source. This was attributed to the resistance to the flow offered by the porous layer and the reduced strength of the vortices inside the enclosure. This pattern did not appear when increasing the Rayleigh number to  $10^7$ , as shown in FIG.13(b), where there is an asymmetric temperature distribution along the heat source when  $0.1 \leq S \leq 0.9$ , while there is a symmetrical distribution when  $S = 0$  and 1 due to the symmetrical vortices' behaviour within the enclosure. It was clear that the heat source temperature at  $Ra = 10^4$  was higher than that at  $Ra = 10^7$ .

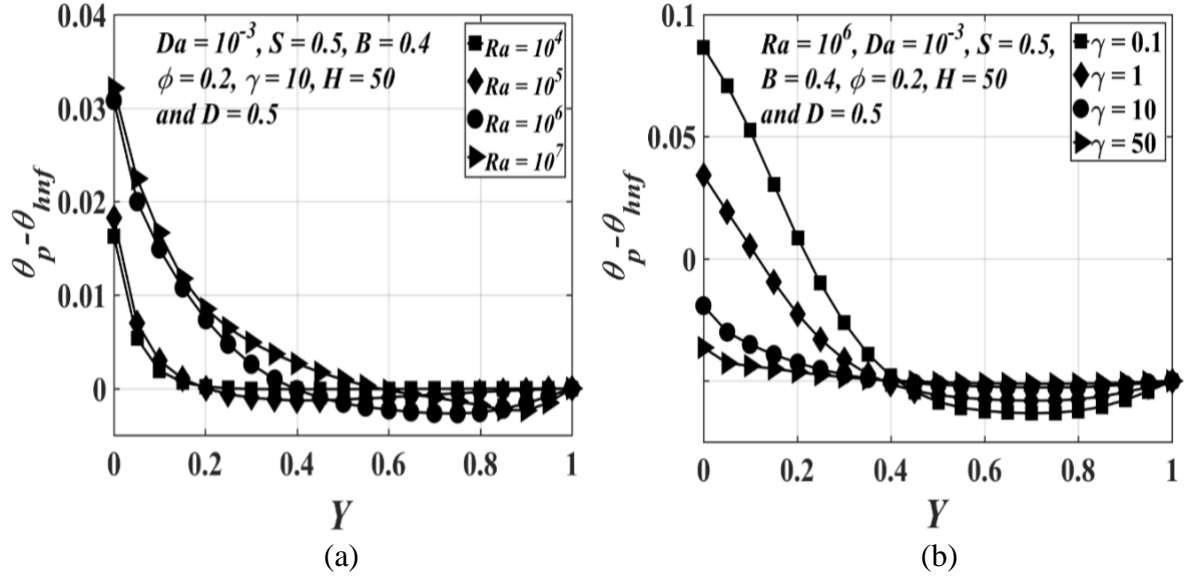


FIG. 12. Variation of solid-to-fluid temperature at the interface vertical mid-plane of the domain ( $X = 0.5$ ) for different values of (a) Rayleigh number (b) thermal conductivity ratio.

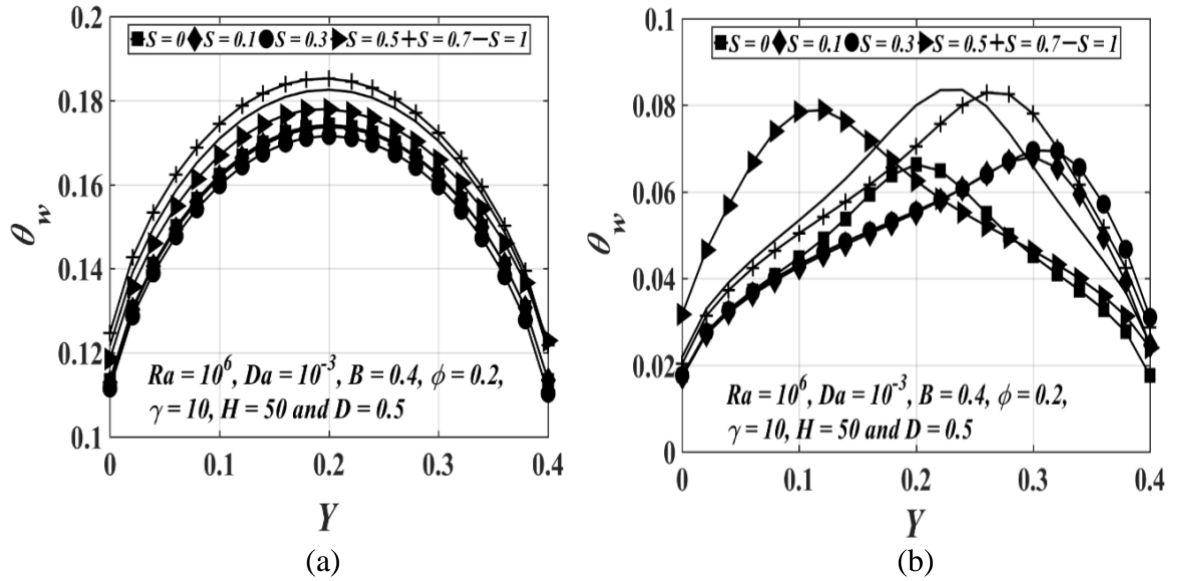


FIG. 13. Variation of dimensionless temperature along the heat source with different porous layer thickness values when (a)  $Ra = 10^4$  and (b)  $Ra = 10^7$ .

### C. Heat transfer rate: Local Nusselt number

Figure 14 depicts the variation of the local Nusselt number along the heat source with different heat source lengths at  $Ra = 10^6$ ,  $Da = 10^{-3}$ ,  $S = D = 0.5$ ,  $\gamma = 50$  and  $H = 50$ . This figure shows asymmetric profiles for the local Nusselt number along the heat source for all lengths of the

heat source,  $B$ . The resultant behaviour exhibits a different pattern to the previous numerical results for the local Nusselt number presented by Bourantas, *et al.*<sup>29</sup> due to the effects of partially filling the enclosure with the porous medium in the present study. The new results show that the heat transfer along the heat source was found to take an asymmetric pattern and the highest and lowest local Nusselt numbers were obtained at the ends and at the porous layer near the interface line, respectively. This was attributed to the flow resistance offered by the porous layer with lower heat transfer rates compared to the fluid layer, where the vortices in the fluid layer have a higher strength of the streamlines compared to the porous layer. Increasing the length of heat source led to a decrease in the local Nusselt number due to the increased heat generation along the heat source.

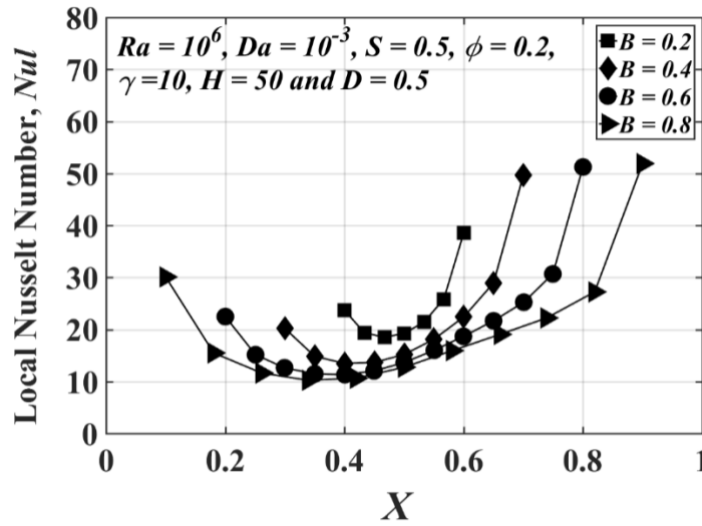


FIG. 14. Variation of local Nusselt number with different heat source length values.

#### D. Overall heat transfer and average $Nu_{av}$

It is known that increasing the thickness of the porous medium reduces the heat transfer rate ( $Nu_{av}$ ); however, in this study, with the selected boundary conditions at the lower value of  $Ra$  using different volume fractions, increasing the porous layer thickness to  $S = 0.3$  was found to enhance the heat transfer rate, as shown in FIG.15(a). This was attributed to the significant increase in streamline strength of the main vortex inside the fluid layer, which increased the ability of the porous medium to receive the heat from the heat source due to the higher heat exchange between the porous and the hybrid nanofluid. Thus, this led to a reduction in the temperature of the heat source. This pattern of  $Nu_{av}$  with porous layer thickness disappeared at higher Rayleigh numbers of  $Ra = 10^7$ , as shown in FIG.15(b). Further increases in  $S$  resulted



in a steady decrease in  $Nu_{av}$ . This was because of the reduction in magnitude of the main vortex stemming from the additional resistance offered by the increased thickness of the porous layer. The reduction in heat transfer rates due to the increased thickness of the porous layer can be overcome by increasing the nanoparticle volume fraction, leading to the improved thermal conductivity of the hybrid nanofluid. Table III shows the heat gain with increasing nanoparticle volume fraction for different values of  $S$  at  $Ra = 10^4$ . At a constant volume fraction, a relative increase in the heat gain with  $S$  up to  $S = 0.3$  was noted; thereafter, with increasing  $S$  up to  $S = 1$ , the heat gains were found to steadily reduce to a minimum at  $S = 0.7$ . For all values of  $S$ , a significant increase in heat gain was found to occur with increasing nanoparticle volume fraction ( $\phi$ ) especially at  $S = 0.3$ . At  $S = 0.3$ , the maximum percentage of the heat gain was 39.69%, and was 62.88% when  $\phi$  was increased to 0.1 and 0.2, respectively, which shows that the improvement in the heat gain was greater than that for the pure fluid.

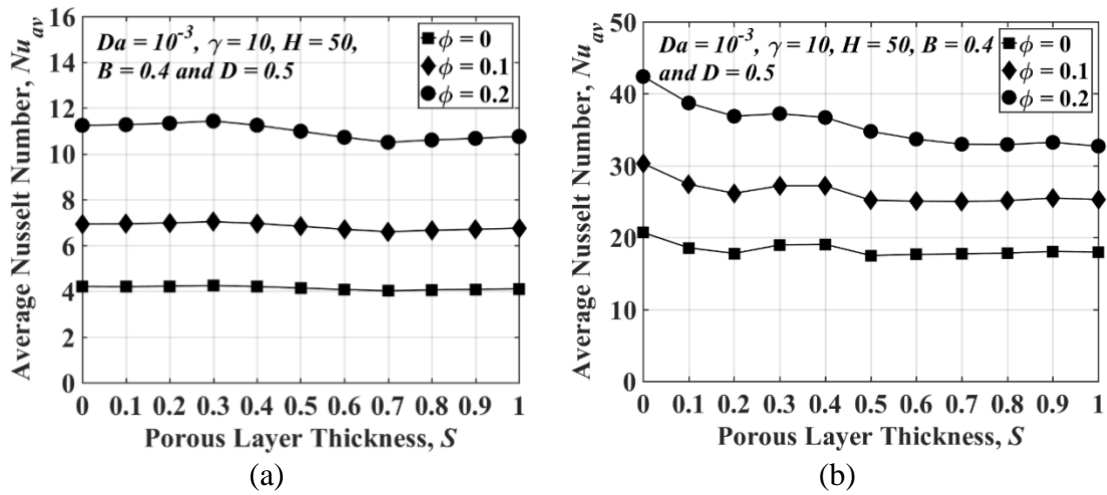


FIG. 15. Variation of average Nusselt number with porous layer thickness for different values of nanoparticles volume fraction at (a)  $Ra = 10^4$ , and (b)  $Ra = 10^7$ .

TABLE III. Heat gain of average Nusselt number with different  $\phi$  and  $S$  values at  $Ra = 10^4$ .

$\phi \backslash S$	0	0.3	0.7	1
0	4.206	4.243	4.0178	4.1096
$Nu_{av}$ increase %	0	0	0	0
0.1	6.933	7.036	6.597	6.7536
$Nu_{av}$ increase %	39.33	39.69	39.09	39.15
0.2	11.243	11.432	10.503	10.757
$Nu_{av}$ increase %	62.59	62.88	61.74	61.8

Figure.16 shows the relationship between  $Nu_{av}$  and Darcy number for different values of  $\gamma$ . Significant increases in the heat transfer rates were found to appear as  $\gamma$  was increased from 0.1 to 10, especially at the higher and lower Darcy numbers. The figure shows that the convective heat transfer starts when  $Da \geq 10^{-5}$  and rapidly increases up to  $\geq 10^{-1}$ . There was no apparent benefit by reducing  $Da$  to less than  $10^{-5}$ , where there was no enhancement in the heat transfer rate. However, increasing the value of  $\gamma$  can improve the heat transfer rate, which was found to give a greater enhancement at lower and higher Darcy numbers than in the range

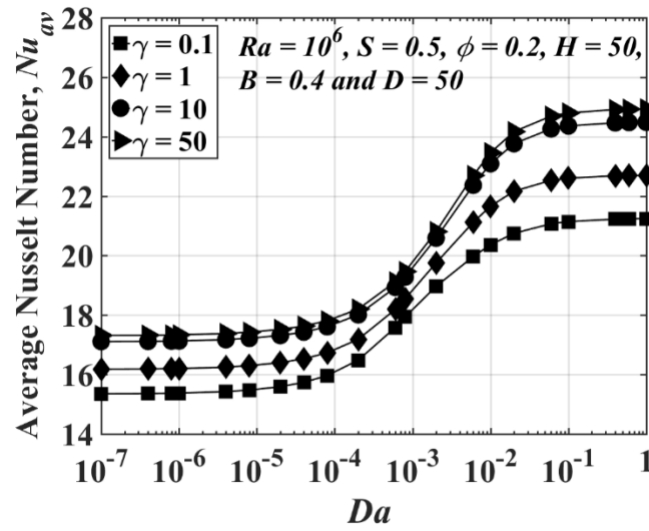


FIG. 16. Variation of average Nusselt number with versus the Darcy number for different thermal conductivity ratio values.

$10^{-4} \leq Da \leq 10^{-2}$ . The enhancement in  $Nu_{av}$  at high  $Da$  is clearer with increasing  $\gamma$ . This is due to the fact that a larger  $Da$  allows the flow to be freely accelerated within the porous layer compared to a lower  $Da$ .

Figure 17 depicts the variation of average Nusselt number with Rayleigh number for different isoflux source lengths in both the pure and hybrid nanofluids. At constant  $B$ , the heat transfer rate increases with increasing the Rayleigh number. In the presence of the hybrid nanofluid,  $Nu_{av}$  was found to greater than that for the pure fluid. At  $B = 0.2$  and  $1$ ,  $Nu_{av}$  seemed to be larger than at  $B = 0.4$  and  $0.8$  for both the pure fluid and the hybrid nanofluid. The increases in  $Nu_{av}$  at  $B = 0.2$  and  $1$  compared to the other lengths is also illustrated in FIG.18. A significant reduction in heat transfer rate was found to occur when  $B$  was increased from  $0.2$  to  $0.8$ . Increasing  $B > 0.8$  caused a steep increase in the heat transfer rate for both the hybrid nanofluid and solid phases.  $Nu_{av}$  is inversely proportional to the heat source temperature. Increasing the length of the heat source led to an increase in the temperature of the fluid and solid phases, as

shown in FIG.10. However, the maximum heat transfer rate found at  $B = 0.2$  and 1 stems from the fact that at  $B = 0.2$ , the fluid inside the enclosure could cool the heated source due to its

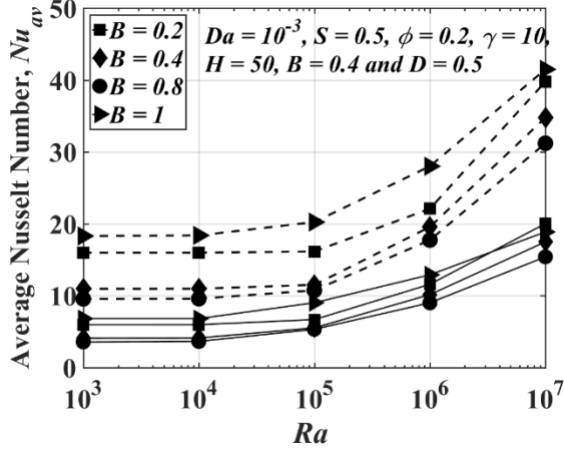


FIG.17. Variation of average Nusselt number versus the Rayleigh number for different heat source length values with pure fluid (solid line) and Hybrid nanofluid (dashed line).

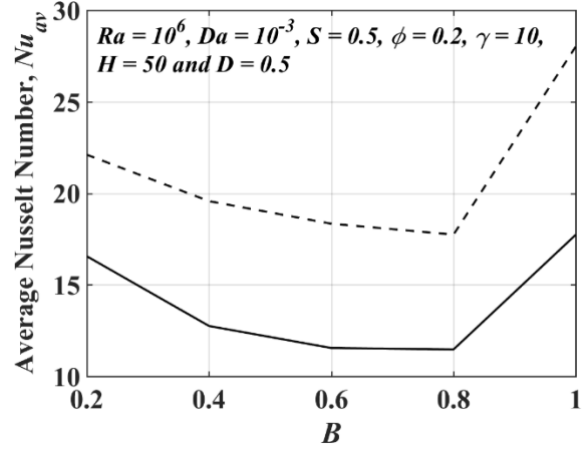


FIG. 18. Variation of average Nusselt number versus the heat source length with solid phase of the porous medium (solid line) and Hybrid nanofluid (dashed line).

low temperature, despite the lower streamline strength than at  $B = 1$ , and despite the higher temperature of the heat source. This figure also shows that  $Nu_{av}$  for the hybrid nanofluid phase are higher than those of the solid phase. This is indicative of thermal non-equilibrium between the hybrid nanofluid and solid phases.

In this study, to illustrate the ideal case of heat exchange between the solid and hybrid nanofluid phases, and to satisfy the equilibrium case between them, FIG.19 shows the variation of  $Nu_{av}$  with  $H$  for different  $\gamma$ .  $H$  is a measure of the solid/hybrid nanofluid scaled heat transfer coefficient, which shows that the substantial difference in the results for the heat transfer rate between the solid and hybrid nanofluid phases that occurs at lower  $H$  is indicative of thermal non-equilibrium between the phases. This means that at small  $H$ , the thermal non-equilibrium case is satisfied. At constant  $\gamma$ , as  $H$  increases the thermal equilibrium case is satisfied and the hybrid nanofluid and solid phases are almost identical, being almost convergent in  $Nu_{av}$ . The variation in heat transfer rate for the hybrid nanofluid and solid phases with  $\gamma$  is shown in FIG.20 for different  $H$  (0.1 - 500). This figure illustrates the fact that a large  $\gamma$  results in the equilibrium case between the hybrid nanofluid and the solid phases. This figure also shows that due to the convection process, increasing  $H$  leads to increased heat transfer in the solid phase due to the decrease in the temperature of the solid, while the heat transfer decreases in the

hybrid nanofluid phase due to the increased hybrid nanofluid temperature. The  $Nu_{av}$  values are much higher for the hybrid nanofluid than those for the solid phase due to the surface contact between the porous medium material and the bottom heated source.

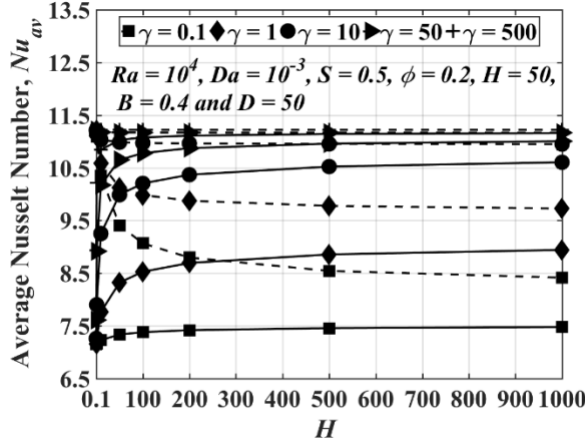


FIG.19. Variation of average Nusselt number versus the interface heat transfer coefficient for different thermal conductivity ratio values with solid phase of the porous medium (solid line) and Hybrid nanofluid (dashed line).

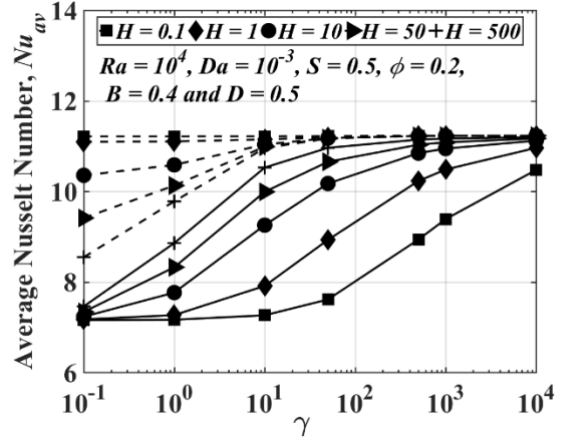


FIG. 20. Variation of average Nusselt number versus the thermal conductivity ratio values for different interface heat transfer coefficient with solid phase of the porous medium (solid line) and Hybrid nanofluid (dashed line).

## V. CONCLUSIONS

Steady-state natural convection inside an enclosure that has been partly filled with a porous medium saturated with a hybrid nanofluid has been investigated using numerical methods via the thermal non-equilibrium model under the influence of discrete isoflux bottom heating. The Darcy–Brinkmann model was used to adopt the governing equations in the porous layer. The Galerkin finite element method was used, with results obtained in terms of streamlines, isotherms and heat transfer over wide ranges of the governing parameters such as the Rayleigh number ( $10^3 \leq Ra \leq 10^7$ ), the Darcy number ( $10^{-7} \leq Da \leq 1$ ), the porous layer thickness ( $0 \leq S \leq 1$ ), the modified thermal conductivity ratio ( $10^{-1} \leq \gamma \leq 10^4$ ) and the interphase heat transfer coefficient ( $10^{-1} \leq H \leq 1000$ ). The choice of the length of the heat source ( $B$ ) was parameterized as 0.2, 0.4, 0.6, 0.8 and 1, with the source itself located at the bottom wall at a fixed location from the sidewall of  $D = 0.5$ . The selected nanoparticle volume fraction was set between  $\phi = 0 - 0.2$ . Some of the important conclusions of this study can be summarised as follows:

- Due to the thermal boundary conditions applied, two anticlockwise vortices with asymmetric distributions along the heat source were generated at the porous and the fluid

layers; the primary vortex occupied the fluid layer while the secondary vortex was located in the porous layer. In addition, the stream function strength increased with increasing the Rayleigh and Darcy numbers.

- Increasing the Rayleigh number and reducing the modified thermal conductivity ratio led to an increase in the resultant velocity and temperature difference between the solid and hybrid nanofluid phases (non-equilibrium case), especially when  $Ra > 10^5$  and  $\gamma < 1$ .
- Increasing the length of the heat source reduced the local Nusselt number with an asymmetric distribution along the heat source itself due to the flow resistance from the porous layer compared to the fluid layer.
- Increasing the thickness of the porous medium from 0 to 0.3 increased the strength of the stream function, resulting in greater heat removal from the heat source while a low intensity was observed for the stream function with an increased thickness of the porous medium. The heat gain from the heat transfer rate at  $S = 0.3$  and  $Ra = 10^4$  increased with increasing volume fraction  $\phi = 0, 0.1$  and  $0.2$ , reaching 0, 39.69% and 62.88%, respectively, which was a higher gain than those recorded for  $S = 0$ .
- Increasing the Darcy number ( $Da > 10^{-5}$ ) enhanced the heat transfer rate resulting from the high permeability of the fluid flow through the porous medium, while at lower Darcy numbers ( $Da \leq 10^{-5}$ ) the heat transfer rate could be improved by increasing the modified thermal conductivity ratio,  $\gamma$ .
- At small values of  $\gamma$ , increasing  $H$  led to an increased heat transfer rate for the solid phase but a decrease for the hybrid nanofluid phase due to the heat received by the hybrid nanofluid from the solid phase. Increasing  $\gamma$  and  $H$  enhanced the heat transfer rate and satisfied the thermal equilibrium case.

## ACKNOWLEDGMENTS

The authors would like to thank the Iraqi Ministry of Higher Education and Scientific Research and the University of Babylon for the financial support to conduct this study. The authors would also like to acknowledge the University of Leicester for providing the necessary resources to carry out this study.

## NOMENCLATURES

$b$	= Heat source length, m	Greek symbols	
$B$	= Dimensionless heat source length, $\frac{b}{L}$	$\alpha$	= Thermal diffusivity ( $m^2.s^{-1}$ )
$Cp$	= Specific heat capacity ( $J.kg^{-1}K^{-1}$ )	$\beta$	= Thermal expansion coefficient ( $K^{-1}$ )
$d$	= Heat source position, m	$\varepsilon$	= Porosity
$D$	= Dimensionless heat source position, $\frac{d}{L}$	$\gamma$	= Modified hybrid nanofluid/porous thermal conductivity ratio
$Da$	= Darcy Number	$\mu$	= Dynamic viscosity ( $Pa.s$ )
$g$	= Gravitational field ( $m.s^{-2}$ )	$\vartheta$	= Kinematic viscosity ( $m^2.s^{-1}$ )
$h$	= Heat transfer coefficient ( $W.m^{-2}.K^{-1}$ )	$\phi$	= Volume fraction of nanoparticles
$H$	= Interphase heat transfer coefficient	$\psi$	= Stream function ( $m^2.s^{-1}$ )
$k$	= Thermal conductivity ( $W.m^{-1}K^{-1}$ )	$\Psi$	= Dimensionless stream function
$K$	= Permeability of porous medium ( $m^2$ )	$\theta$	= Dimensionless temperature
$L$	= Length of the cavity ( $m$ )	$\rho$	= Density ( $kg.m^{-3}$ )
$Nu$	= Nusselt number	Subscript	
$p$	= Pressure ( $N.m^{-2}$ )	$av$	= Average
$P$	= Dimensionless pressure	$Al_2O_3$	= Alumina nanoparticles
$Pr$	= Prandtl number	$bf$	= Base fluid
$Ra$	= Rayleigh number	$c$	= Cold
$s$	= Porous layer thickness ( $m$ )	$Cu$	= Copper nanoparticles
$S$	= Dimensionless porous layer thickness, $\frac{s}{L}$	$f$	= Fluid
$T$	= Temperature ( $K$ )	$hnf$	= Hybrid Nanofluid
$u, v$	= Velocity components in the $x$ and $y$ -directions respectively. ( $m.s^{-1}$ )	$p$	= Porous medium region
$U, V$	= Dimensionless velocity components in the $X$ and $Y$ -directions respectively	$w$	= Heat source wall
$x, y$	= Cartesian coordinates ( $m$ )		
$X, Y$	= Dimensionless Cartesian coordinates		

## REFERENCES

1. T. Basak, S. Roy, A. Matta, and I. Pop, "Analysis of heatlines for natural convection within porous trapezoidal enclosures: effect of uniform and non-uniform heating of bottom wall," *International Journal of Heat and Mass Transfer* **53**, 5947 (2010).
2. M. Al-Nimr, and A. Khadrawi, "Transient free convection fluid flow in domains partially filled with porous media," *Transport in porous media* **51**, 157 (2003).
3. A. J. Chamkha, and M. A. Ismael, "Natural convection in differentially heated partially porous layered cavities filled with a nanofluid," *Numerical Heat Transfer, Part A: Applications* **65**, 1089 (2014).
4. M. A. Ismael, and A. J. Chamkha, "Conjugate natural convection in a differentially heated composite enclosure filled with a nanofluid," *Journal of Porous Media* **18**, (2015).
5. P. Cheng, "Heat transfer in geothermal systems," *Advances in heat transfer* **14**, 1 (1978).

6. D. A. Nield, and A. Bejan, *Convection in porous media* (Springer Science & Business Media, 2006).
7. V. Kumar, "Coupling of free flow and flow in porous media—a dimensional analysis," Forschungsbericht, Institut für Wasserbau, Lehrstuhl für Hydromechanik und Hydrosystemmodellierung, Universität Stuttgart (2011).
8. A. Bagchi, and F. A. Kulacki, *Natural Convection in Superposed Fluid-Porous Layers* (Springer, 2014).
9. K. L. Walker, and G. M. Homsy, "Convection in a porous cavity," *J. Fluid Mech* **87**, 449 (1978).
10. J. M. de Medeiros, F. Marcondes, and J. M. Gurgel, "Natural convection in a porous cavity using the generalized model with uniform porosity," (1999).
11. M. C. Kim, S. B. Lee, S. Kim, and B. J. Chung, "Thermal instability of viscoelastic fluids in porous media," *International journal of heat and mass transfer* **46**, 5065 (2003).
12. M. E. Ismaeel, "Heat Transfer in a Square Porous Cavity With Partial Heating and Cooling for Opposite Vertical Walls," *Al-Rafadain Engineering Journal* **19**, (2011).
13. M. Muthamilselvan, "Analysis of Heat and Mass Transfer in a Porous Cavity Containing Water near Its Density Maximum," *Applied Mathematics* **2**, 927 (2011).
14. A. Tiwari, A. Singh, P. Chandran, and N. Sacheti, "Natural convection in a cavity with a sloping upper surface filled with an anisotropic porous material," *Acta Mechanica* **223**, 95 (2012).
15. A. Fard, B. Ghasemi, and M. Kohyani, "Heat generation effects on natural convection in porous cavity with different walls temperature," *Frontiers in Heat and Mass Transfer (FHMT)* **3**, (2012).
16. D. Poulikakos, A. Bejan, B. Selimos, and K. Blake, "High Rayleigh number convection in a fluid overlaying a porous bed," *International Journal of Heat and Fluid Flow* **7**, 109 (1986).
17. N. Tatsuo, T. Toru, S. Mitsuhiro, K. Yuji, and O. Hiroyuki, "Numerical analysis of natural convection in a rectangular enclosure horizontally divided into fluid and porous regions," *International journal of heat and mass transfer* **29**, 889 (1986).
18. P. Vasseur, C. Wang, and M. Sen, "Thermal instability and natural convection in a fluid layer over a porous substrate," *Wärme-und Stoffübertragung* **24**, 337 (1989).
19. F. Arpino, N. Massarotti, and A. Mauro, "Efficient three-dimensional FEM based algorithm for the solution of convection in partly porous domains," *International Journal of Heat and Mass Transfer* **54**, 4495 (2011).
20. T. Tong, and E. Subramanian, "Natural convection in rectangular enclosures partially filled with a porous medium," *International journal of heat and fluid flow* **7**, 3 (1986).

21. C. Beckermann, S. Ramadhyani, and R. Viskanta, "Natural convection flow and heat transfer between a fluid layer and a porous layer inside a rectangular enclosure," *Journal of heat transfer* **109**, 363 (1987).
22. S. Sathe, W.-Q. Lin, and T. Tong, "Natural convection in enclosures containing an insulation with a permeable fluid-porous interface," *International journal of heat and fluid flow* **9**, 389 (1988).
23. N. Putra, W. Roetzel, and S. K. Das, "Natural convection of nano-fluids," *Heat and Mass Transfer* **39**, 775 (2003).
24. H. Saleh, R. Roslan, and I. Hashim, "Natural convection heat transfer in a nanofluid-filled trapezoidal enclosure," *International Journal of Heat and Mass Transfer* **54**, 194 (2011).
25. R. Roslan, H. Saleh, and I. Hashim, "Effect of rotating cylinder on heat transfer in a square enclosure filled with nanofluids," *International Journal of Heat and Mass Transfer* **55**, 7247 (2012).
26. S. S. Rao, and A. Srivastava, "Interferometric study of natural convection in a differentially-heated cavity with Al<sub>2</sub>O<sub>3</sub>-water based dilute nanofluids," *International Journal of Heat and Mass Transfer* **92**, 1128 (2016).
27. C. Grobler, M. Sharifpur, H. Ghodsinezhad, R. Capitani, and J. Meyer, "Experimental study on cavity flow natural convection in porous medium, saturated with an Al (sub2) O (sub3) 60% EG-40% water nanofluid," (2015).
28. R. Chand, and G. Rana, "On the onset of thermal convection in rotating nanofluid layer saturating a Darcy–Brinkman porous medium," *International Journal of Heat and Mass Transfer* **55**, 5417 (2012).
29. G. Bourantas, E. Skouras, V. Loukopoulos, and V. Burganos, "Heat transfer and natural convection of nanofluids in porous media," *European Journal of Mechanics-B/Fluids* **43**, 45 (2014).
30. T. Groşan, C. Revnic, I. Pop, and D. Ingham, "Free convection heat transfer in a square cavity filled with a porous medium saturated by a nanofluid," *International Journal of Heat and Mass Transfer* **87**, 36 (2015).
31. M. T. Nguyen, A. M. Aly, and S.-W. Lee, "Natural convection in a non-darcy porous cavity filled with Cu–water nanofluid using the characteristic-based split procedure in finite-element method," *Numerical Heat Transfer, Part A: Applications* **67**, 224 (2015).
32. A. Chamkha, A. Rashad, M. Mansour, T. Armaghani, and M. Ghalambaz, "Effects of heat sink and source and entropy generation on MHD mixed convection of a Cu-water nanofluid in a lid-driven square porous enclosure with partial slip," *Physics of Fluids* **29**, 052001 (2017).
33. M. Sheikholeslami, and H. B. Rokni, "Magnetic nanofluid flow and convective heat transfer in a porous cavity considering Brownian motion effects," *Physics of Fluids* **30**, 012003 (2018).
34. M. Sheikholeslami, and S. Shehzad, "CVFEM simulation for nanofluid migration in a porous medium using Darcy model," *International Journal of Heat and Mass Transfer* **122**, 1264 (2018).



35. S. H. Hussain, and M. S. Rahomey, "Comparison of Natural Convection around a Circular Cylinder with Different Geometries of Cylinders inside a Square Enclosure Filled with Ag-Nanofluid Superposed Porous-Nanofluid Layers," (2018).
36. J. Sarkar, P. Ghosh, and A. Adil, "A review on hybrid nanofluids: recent research, development and applications," *Renewable and Sustainable Energy Reviews* **43**, 164 (2015).
37. N. A. C. Sidik, I. M. Adamu, M. M. Jamil, G. Kefayati, R. Mamat, and G. Najafi, "Recent progress on hybrid nanofluids in heat transfer applications: a comprehensive review," *International Communications in Heat and Mass Transfer* **78**, 68 (2016).
38. R. R. Sahoo, P. Ghosh, and J. Sarkar, "Performance Analysis of a Louvered Fin Automotive Radiator Using Hybrid Nanofluid as Coolant," *Heat Transfer—Asian Research* **46**, 978 (2017).
39. J. R. Babu, K. K. Kumar, and S. S. Rao, "State-of-art review on hybrid nanofluids," *Renewable and Sustainable Energy Reviews* **77**, 551 (2017).
40. M. Ghalambaz, A. Doostani, E. Izadpanahi, and A. Chamkha, "Phase-change heat transfer in a cavity heated from below: The effect of utilizing single or hybrid nanoparticles as additives," *Journal of the Taiwan Institute of Chemical Engineers* **72**, 104 (2017).
41. S. Ghadikolaei, M. Yassari, H. Sadeghi, K. Hosseinzadeh, and D. Ganji, "Investigation on thermophysical properties of  $\text{TiO}_2\text{-Cu/H}_2\text{O}$  hybrid nanofluid transport dependent on shape factor in MHD stagnation point flow," *Powder Technology* **322**, 428 (2017).
42. S. Suresh, K. Venkitaraj, P. Selvakumar, and M. Chandrasekar, "Synthesis of  $\text{Al}_2\text{O}_3\text{-Cu}$ /water hybrid nanofluids using two step method and its thermo physical properties," *Colloids and Surfaces A: Physicochemical and Engineering Aspects* **388**, 41 (2011).
43. P. Jena, E. Brocchi, and M. Motta, "In-situ formation of  $\text{Cu-Al}_2\text{O}_3$  nano-scale composites by chemical routes and studies on their microstructures," *Materials Science and Engineering: A* **313**, 180 (2001).
44. M. J. Nine, B. Munkhbayar, M. S. Rahman, H. Chung, and H. Jeong, "Highly productive synthesis process of well dispersed  $\text{Cu}_2\text{O}$  and  $\text{Cu/Cu}_2\text{O}$  nanoparticles and its thermal characterization," *Materials Chemistry and Physics* **141**, 636 (2013).
45. T. T. Baby, and R. Sundara, "Synthesis and transport properties of metal oxide decorated graphene dispersed nanofluids," *The Journal of Physical Chemistry C* **115**, 8527 (2011).
46. B. Takabi, and S. Salehi, "Augmentation of the heat transfer performance of a sinusoidal corrugated enclosure by employing hybrid nanofluid," *Advances in Mechanical Engineering* **6**, 147059 (2014).
47. A. J. Chamkha, I. V. Miroshnichenko, and M. A. Sheremet, "Numerical Analysis of Unsteady Conjugate Natural Convection of Hybrid Water-Based Nanofluid in a Semicircular Cavity," *Journal of Thermal Science and Engineering Applications* **9**, 041004 (2017).
48. R. S. R. Gorla, S. Siddiq, M. Mansour, A. Rashad, and T. Salah, "Heat Source/Sink Effects on a Hybrid Nanofluid-Filled Porous Cavity," *Journal of Thermophysics and Heat Transfer* (2017).

49. F. Wu, W. Zhou, and X. Ma, "Natural convection in a porous rectangular enclosure with sinusoidal temperature distributions on both side walls using a thermal non-equilibrium model," *International Journal of Heat and Mass Transfer* **85**, 756 (2015).
50. A. C. Baytas, and I. Pop, "Free convection in a square porous cavity using a thermal nonequilibrium model," *International Journal of Thermal Sciences* **41**, 861 (2002).
51. A. Baytas, "Thermal non-equilibrium natural convection in a square enclosure filled with a heat-generating solid phase, non-Darcy porous medium," *International journal of energy research* **27**, 975 (2003).
52. S. Khashan, A. Al-Amiri, and I. Pop, "Numerical simulation of natural convection heat transfer in a porous cavity heated from below using a non-Darcian and thermal non-equilibrium model," *International Journal of Heat and Mass Transfer* **49**, 1039 (2006).
53. I. A. Badruddin, Z. Zainal, P. A. Narayana, and K. Seetharamu, "Numerical analysis of convection conduction and radiation using a non-equilibrium model in a square porous cavity," *International journal of thermal sciences* **46**, 20 (2007).
54. F. Wu, G. Wang, and W. Zhou, "Buoyancy induced convection in a porous cavity with sinusoidally and partially thermally active sidewalls under local thermal non-equilibrium condition," *International Communications in Heat and Mass Transfer* **75**, 100 (2016).
55. M. A. Sheremet, I. Pop, and R. Nazar, "Natural convection in a square cavity filled with a porous medium saturated with a nanofluid using the thermal nonequilibrium model with a Tiwari and Das nanofluid model," *International Journal of Mechanical Sciences* **100**, 312 (2015).
56. A. Alsabery, H. Saleh, I. Hashim, and P. Siddheshwar, "Transient natural convection heat transfer in nanoliquid-saturated porous oblique cavity using thermal non-equilibrium model," *International Journal of Mechanical Sciences* **114**, 233 (2016).
57. M. Sabour, and M. Ghalambaz, "Natural convection in a triangular cavity filled with a nanofluid-saturated porous medium using three heat equation model," *Canadian Journal of Physics* **94**, 604 (2016).
58. A. Alsabery, A. Chamkha, I. Hashim, and P. Siddheshwar, "Effects of Nonuniform Heating and Wall Conduction on Natural Convection in a Square Porous Cavity Using LTNE Model," *Journal of Heat Transfer* **139**, 122008 (2017).
59. M. Izadi, G. Hoghoughi, R. Mohebbi, and M. Sheremet, "Nanoparticle migration and natural convection heat transfer of Cu-water nanofluid inside a porous undulant-wall enclosure using LTNE and two-phase model," *Journal of Molecular Liquids* **261**, 357 (2018).
60. M. A. Sheremet, and I. Pop, "Effect of local heater size and position on natural convection in a tilted nanofluid porous cavity using LTNE and Buongiorno's models," *Journal of Molecular Liquids* (2018).
61. S. Aminossadati, and B. Ghasemi, "Natural convection cooling of a localised heat source at the bottom of a nanofluid-filled enclosure," *European Journal of Mechanics-B/Fluids* **28**, 630 (2009).

62. T. Basak, S. Roy, and H. S. Takhar, "Effects of nonuniformly heated wall (s) on a natural-convection flow in a square cavity filled with a porous medium," *Numerical Heat Transfer, Part A: Applications* **51**, 959 (2007).